# SPATIAL STRUCTURE OF THERMOCLINE AND ABYSSAL INTERNAL WAVES

Thomas B. Sanford

Applied Physics Laboratory, College of Ocean and Fishery Sciences, University of Washington, Seattle, WA 98105-6698

## ABSTRACT

One hundred velocity profiles over nearly the entire water column are analyzed in terms of the vertical and horizontal structure of the steady and internal-wave velocity contributions. The temporal decomposition into steady, inertial, and high-frequency internal-wave contributions is obtained from several brief time series at one location. The spatial structure of the velocity field is obtained from simultaneous profiles at separations ranging from 15 m to 15 km. WKB normalization of wave amplitude and stretching of vertical wavenumber are performed on the inertial and internal wave components. A reference Brunt-Väisälä frequency ($N_0$) of 3 cph is used. Spectra are computed on the WKB scaled profiles over more than 90% of the water column and separately over the upper and lower halves. The total internal wave field exhibits equipartition between the east and north velocity components, a decrease in energy density at the lowest wavenumber, and an overall dependence of KE on vertical wavenumber ($m$) as $m^{-2.5}$. Most of the internal wave energy is contributed by inertial motions, and of this most occurs at (scaled) wavelengths of 100–500 m with a peak at mode 3 (500-m wavelength). The inertial period contributions reveal a power law of $m^{-3}$, while the high-frequency internal waves ($\omega > 2f$) follow a slope of $m^{-2}$. There is strong vertical polarization (CW > ACW) of the near-inertial contribution but little or none for the higher-frequency motions. The scaled water column is divided in half for upper-half/lower-half comparisons. There is more scaled inertial KE in the lower half of the water column. The high-frequency internal waves have comparable total energy, but the upper-half spectrum shows a deficiency (or the lower half shows an excess) at vertical wavelengths shorter than 100 stretched meters. The upper half is where the time-mean shear is largest and critical layer processes might be playing a significant role. On the other hand, the lower half may exhibit the influences of bottom scattering of internal waves which tend to "whiten" the spectrum. A few simultaneous, but spatially separated, velocity profiles are differenced, and the KE of the resulting profiles have a zero-correlation scale of about 15–20 km for the total internal wave field. The difference profiles consist primarily of inertial waves. Thus, the deep water inertial waves exhibit wavelengths of 60–80 km (four times the zero-correlation distance) or less in contrast to much longer scales reported for the SML and uppermost thermocline.

## 1. INTRODUCTION

The least measured aspect of oceanic internal waves is the spatial structure. This is especially true in the abyssal oceans. The paucity of velocity observations there reflects more the difficulty in making appropriate measurements than a lack of interest in or recognition of the importance of the spatial structure. Regardless of the cause, ignorance of the horizontal variability of the velocity field is profound. This is an unfortunate circumstance, because there are

109

numerous reasons to study the spatial structure of internal wave velocities. The spatial characteristics must be observed to improve our understanding of

- wave dispersion
- effects of advection and Doppler contamination
- WKB scaling and power laws
- wave propagation (momentum, heat, and kinetic energy fluxes)
- wave nonlinearities, such as wave-wave interactions
- wave mixing and instabilities
- interactions of waves and mean currents
- spatial inhomogeneities and patchiness.

Most of the previous spatial studies have been in the upper ocean, and of these most are of temperature. For example, Hayes (1975), Katz (1975), and Stegen et al. (1975) present observations of vertical profile series, horizontal tows, and profile sections, respectively. The pioneering observations in IWEX (Müller et al., 1978) and GATE (Käse and Olbers, 1979) provided important thermocline measurements over a spatial array of moored instruments. Considerable measurements of upper ocean velocity and temperature have been obtained with XCPs (Kunze and Sanford, 1984; D'Asaro, 1984; Kunze and Sanford, 1986). The spatial distribution of inertial waves forced by moving hurricanes is discussed by Sanford et al. (1987). Acoustic Doppler profiling with enhanced depth capabilities has been conducted by Pinkel with great success in the tropical Pacific thermocline. Basically, these various observations do not reach deeper than about 1000 m, the base of the permanent thermocline.

The goals of this work are to describe the dominant vertical and horizontal scales of internal wave variability as revealed in profiles of horizontal velocity. An attempt is made to separate the contribution of inertial- from higher-frequency (i.e., $\omega > 2f$) internal waves and contrast thermocline and abyssal motions. Special attention is given to the observation and analysis of subthermocline internal waves.

## 2. THE OBSERVATIONS

The observations were collected in the Sargasso Sea of the western North Atlantic Ocean, in a region with a relatively flat bottom, at least 400 km from appreciable topographic features (except for drops 306–310, which are not included in the spectra). The observations were taken in 1973 and 1975 during the MODE-I (MODE Group, 1978) and FAME (Sanford and Hogg, 1977) programs. The profile locations are presented in Fig. 1, with additional information contained in Table 1. All the data were taken in the summer and fall in generally light winds and low sea states.

A free-fall velocity profiler operating on the principles of geomagnetic induction (Sanford et al., 1978) was used to profile the entire water column. The device is called an EMVP, for Electro-Magnetic Velocity Profiler. In the water depth involved for these data (5200–5500 m), the EMVP required about 1.5 hours for a down or up traverse of the water column. When operating in a time-series mode, occupying one site repeatedly, the EMVP was deployed about once every 6 hours. A set of seven time series of profiles was analyzed. One series was obtained in shallower water (4500 m) than the other six. The remaining group of six time-series profiles, consisting of 50 drops, or 100 profiles (down and up traverses are used separately), are WKB scaled and spectrally analyzed. A second measurement configuration, intended to reveal horizon-
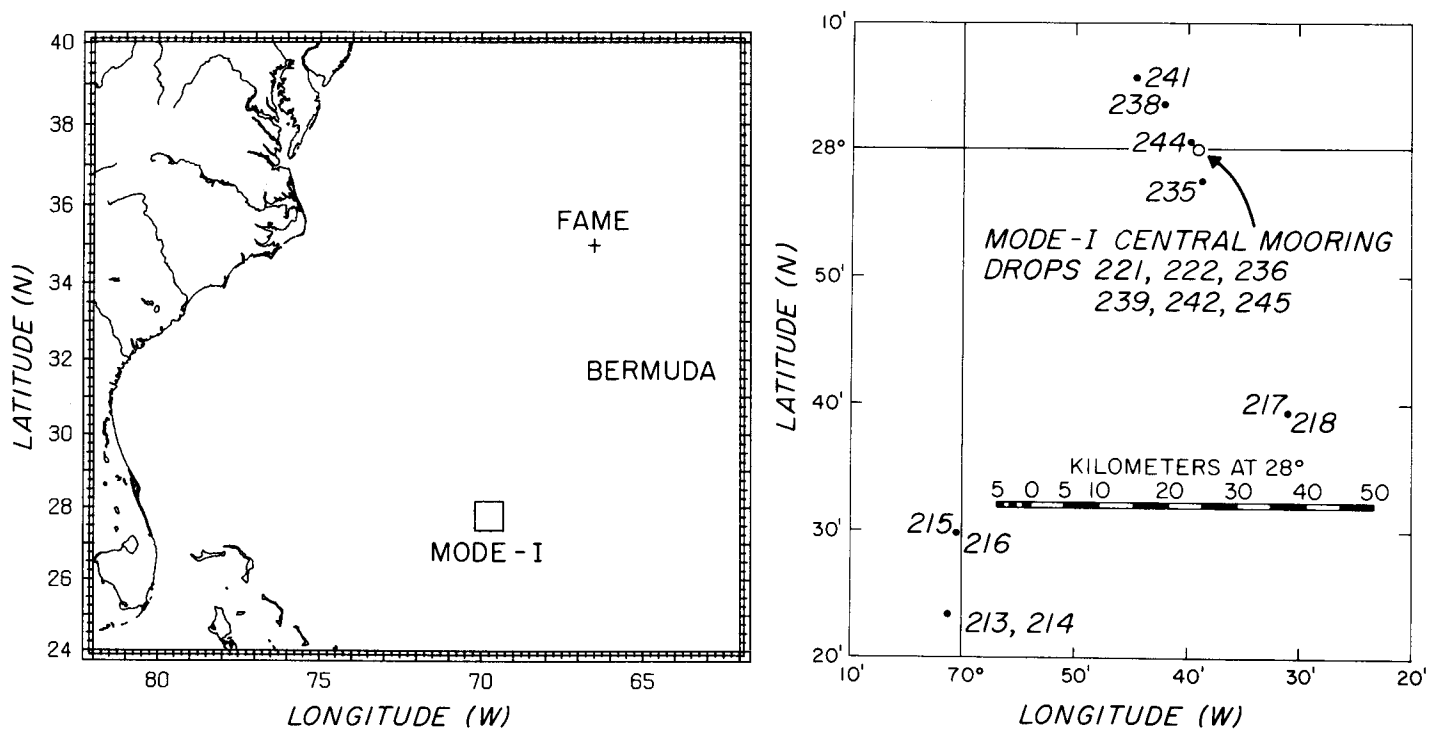
Fig. 1.  Locations of profiles used in this study.  All data were taken in the western North Atlantic in the Sargasso Sea.  The smaller-scale figure shows locations of simultaneous, separated profiles around the MODE-I central mooring.

tal gradients, was deployed in which two EMVPs were preset to fall simultaneously at a known horizontal separation.  Over a dozen such horizontally spaced pairs were obtained, but only four were made at horizontal separations of 1 km or greater.

The data quality is good, with errors not exceeding 1 cm/s rms.  This level is consistent with the analysis of Sanford *et al.* (1978) and the measured rms differences between closely spaced profiles.  The vertical resolution on the original profiles is about 8 dbars, which becomes 10 dbars after interpolation to a uniformly spaced series.

Because of intermittent failures of the internal digital recorder and the application of data quality criteria, gaps exist in some of the profile series.  The recorder-produced gaps seldom exceed 10% on the better recorder, but sometimes 50% of the data is missing on the recorder aboard the second EMVP.  A quality screening is applied to the data, such that if the noise in the EM data exceeds the equivalent of about 1 cm/s rms, no velocity determination is made.  This condition occurred frequently above 100 m depth because of bubble formation in the electrode arms.  When the gaps are short and not too frequent, they are filled by interpolation.  When the gaps are more extensive, the data are not used or, if part of a spatially separated pair, only measured points are used.

The horizontal spacing between two simultaneously dropped profilers was determined acoustically using synchronized acoustic transmissions from the two profilers.  Travel times for

111

Table 1. Profiles used in analysis.

| Group | Type | Location |
|-------|------|----------|
| 202-206 | Time Series | 27° 58′ N  69° 38′ W |
| 213-214 | Spaced Drops | 27° 23′ N  70° 01′ W |
| 215-216 | Spaced Drops | 27° 29′ N  70° 00′ W |
| 217-218 | Spaced Drops | 27° 39′ N  69° 31′ W |
| 219-228 | Time Series | 28° 00′ N  69° 39′ W |
| 221-222 | Spaced Drops | 28° 00′ N  69° 39′ W |
| 230-245 | Time Series | 28° 00′ N  69° 39′ W |
| 235-236 | Spaced Drops | 28° 00′ N  69° 39′ W |
| 238-239 | Spaced Drops | 28° 00′ N  69° 39′ W |
| 241-242 | Spaced Drops | 28° 00′ N  69° 39′ W |
| 244-245 | Spaced Drops | 28° 00′ N  69° 39′ W |
| 251-260 | Time Series | 35° 00′ N  66° 30′ W |
| 262-274 | Time Series | 35° 00′ N  66° 30′ W |
| 306-310 | Time Series | 32° 58′ N  64° 23′ W |
| 320-324 | Time Series | 35° 00′ N  66° 30′ W |

direct and bottom-reflected acoustic paths were used to determine probe separations. Also, at short separations the distance could be measured visually; at the longest separations (> 4 km) the position of the surface release for the distant EMVP was calculated by interpolation between deployment and recovery positions as determined from LORAN. The displacement of the probe during a profile is negligible compared with that due to the surface current action before and after a profile. For separations of 100 m or less, it was possible to confirm visually that the profilers returned to the surface with approximately the same horizontal separation as at launch.

## 3. DATA ANALYSIS

Most of the kinetic energy of these velocity profiles resides in the low-frequency, quasi-geostrophic motions, with internal waves contributing only about 20% of the total horizontal kinetic energy. Two methods are used to separate the internal waves from the background. In the first method, a 1-day or longer series of profiles at a location is fitted to time-mean and inertial-period components by a rotary, least-square decomposition method described by Sanford (1975). The time-mean profile is subtracted from the individual profiles; the residue profiles are principally composed of internal waves. When both the time-mean and inertial profiles are subtracted from the original profiles, the residue profiles are of higher-frequency internal waves.

The second scheme involves the subtraction of two simultaneous but horizontally separated profiles. The residue profile is taken to be composed of internal waves, since the difference in low-frequency structure over 10 km is assumed to be negligible. This assumption is based on the

measured correlation length of about 100 km for the MODE eddy (MODE Group, 1978). Both methods of internal wave discrimination are barely adequate, yet both permit useful analysis of internal waves in the presence of strong planetary motion.

The third method for removing the time-mean or planetary motion is to fit individual profiles to vertical eigenmodes for linear, flat-bottom, and zero-mean-flow Rossby waves. It was thought that the modal fit would filter out the internal waves. The eigenmodes are solutions to the equation (Pedlosky, 1979)

$$\left[\frac{f^2}{N^2}W_z\right]_z + \lambda W = 0 , \tag{1}$$

where ($W$) is the eigenfunction, the subscript denotes differentiation with respect to depth $z$, and $N$ and $f$ are the Brunt-Väisälä and Coriolis frequencies. The separation constant ($\lambda$) is $-[(-\beta k/\omega) + k^2 + l^2]$, where $\beta$ is the horizontal (meridional) gradient of $f$, $\omega$ is the wave frequency, and $k$ and $l$ are the east and north horizontal wavenumbers. The boundary conditions at the sea surface and bottom are

$$W = 0 \text{ at } z = 0 \text{ and } -H . \tag{2}$$

The hypothesis is that an energetic mode will remain constant from fit to fit, being relatively unaffected by the internal waves. However, it is found that the decompositions show that the modal estimates, even for the most energetic first mode, fluctuate greatly over the brief series. The cause of this behavior is large, low-mode inertial period components that contaminate the eigenmode computation. Eigenmode fitting is very useful, however, when applied to the time-mean profiles derived from the rotary, least-square decomposition.

The time series profiles are decomposed into time-mean, inertial, and high-frequency internal wave components. Since the subinertial motion is so energetic, it is better to remove most of it from the series at the first step. The difference between the original profiles and the arithmetic mean profile is called the internal wave field. The next stage is to subject the total internal wave field to the rotary, least-square demodulation at a frequency equal to $1.05 f$, a dominant frequency often observed in moored current meter records (Webster, 1968). From this procedure are obtained two velocity profiles: the low-frequency (which is small since the arithmetic mean has been removed) and the inertial. The small, low-frequency component is added to the arithmetic mean to yield the best estimate of the subinertial (time-mean) profile. The inertial profile consists essentially of speed and direction values referenced to some arbitrary, prescribed time $t_o$. To compute the inertial profile at a given time $t$, it is necessary to add to the computed direction an amount given by $1.05f$ $(t - t_o)$. Thus the higher-frequency internal wave field is obtained by subtracting the time-mean and the appropriately time-advanced inertial profiles from each of the original profiles.

The independence of the inertial and higher frequency profiles (i.e., lack of correlation) is demonstrated in Appendix A.

Both down and up profiles have been used. No vertical interpolation has been performed; if more than 2/3 of the data at a given 10 dbar level is missing, no fit is performed at that level. That is, if 10 profiles were used (say 202–206, down and up), then 7 or more of the 10 velocity values must be available at that depth level for an acceptable fit to be made.

The fitting for steady and inertial components for the series 202–206 is shown in Fig. 2. This series provides a clear example of the compact description often possible for subinertial profiles. About 95% of the baroclinic energy is contained in the steady profile. The relative smoothness of the steady profile demonstrates the dominance of the steady component and the ability of a few vertical profiles to obtain an adequate determination of the mean flow. Sanford (1975) showed how a pair of velocity profiles taken half an inertial period apart nicely reveals the steady and inertial contributions.
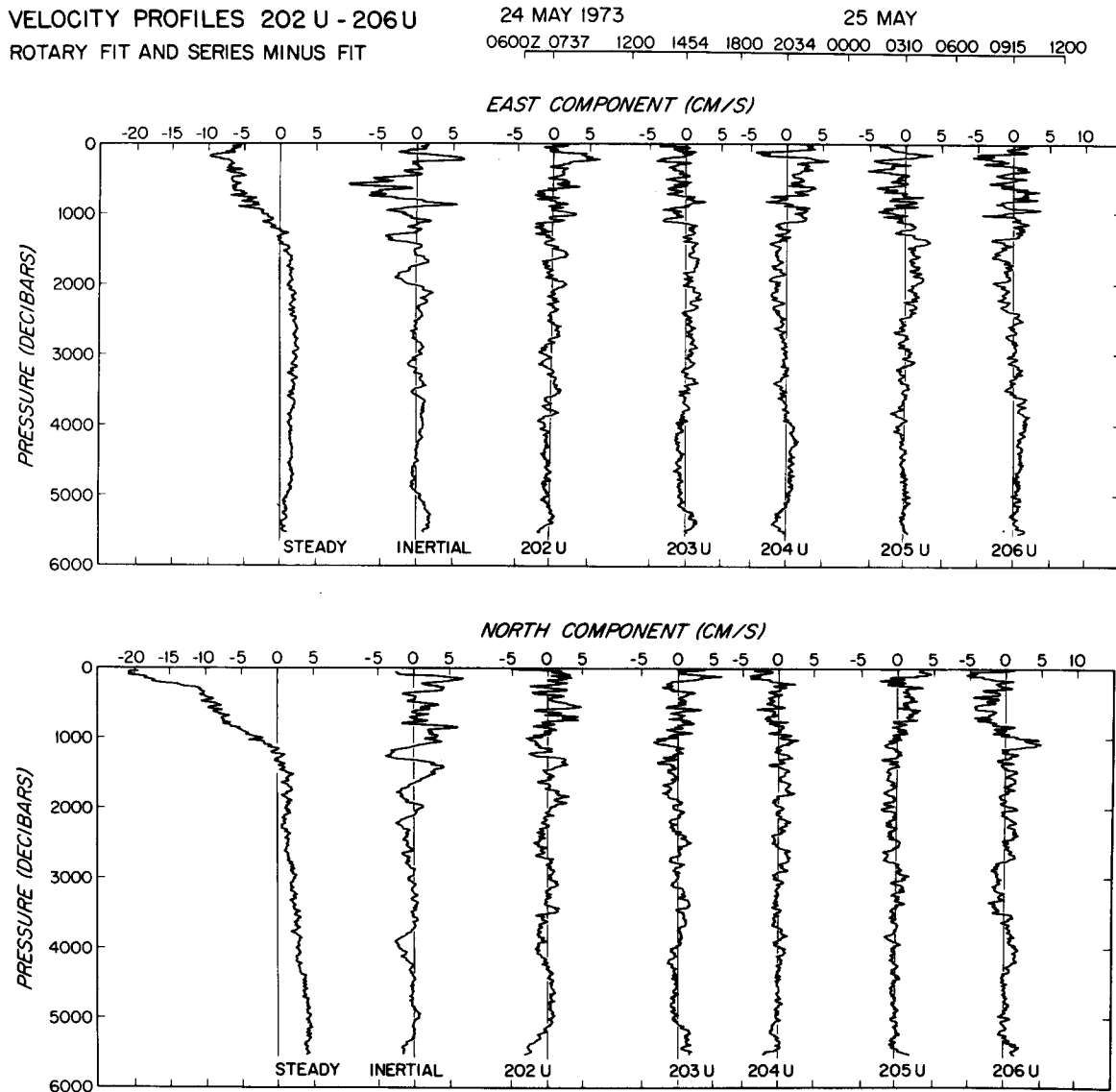


Fig. 2. Estimates at each 10-dbar level of the steady, inertial, and residual profiles (result of removing steady and inertial components from the original profiles). The inertial component was computed at a period of 25.6 hours $(1.05f)$ and is shown for the reference time of 0000 24 May 1973. The drop time of the individual profiles in this series is shown in the upper scale.

The modal composition of the 202–206 steady profile is shown in Fig. 3. Only the first mode is shown in actual magnitude; the higher modes are shown at a magnification of 5. The first mode is the dominant component, with the third adding some near-surface flow.

The time-mean profiles are presented in Fig. 4, and the inertial-period profiles are shown in Fig. 5 for the seven-profile series. The data sets are denoted as 202–206, 219–228, 230–245, 251–260, 262–274, 306–310, and 320–324, where the numbers are the first and last drop numbers used in each series. Note that drops 306–310 are in shallower water, which is still very deep but significantly less than at the other sites.

Two characteristics of these data should be mentioned. First, the time-mean profiles have considerable shear in the upper 1000 m; 320–324 also has higher mode, deeper shears. In general, the vertical shear is much less below 1000–1500 m than in the upper ocean. Second, the inertial fits are not totally independent of each other, and the energy and vertical scales are clearly larger in the FAME data set compared with MODE-I profiles. The two experiments were conducted at different latitudes (28°N vs 35°N), at different seasons (summer vs fall), and under different weather conditions. Profiles obtained in the POLYMODE experiment around 30°N, just north of the MODE-1 site, exhibit low levels of inertial motions. The latitudinal dependence of inertial motions has been investigated by Fu (1981), who found that the inertial peak grows and sharpens with higher latitude. With a small sample, it is not possible to determine if there are seasonal, weather, or latitudinal effects, as opposed to the expected variability due to sampling.

The modal fits for six time series (i.e., Fig. 4 without 262–274) are shown in Fig. 6. The first mode, which is plotted at one-fifth amplitude, is clearly dominant. Only the right-most profiles exhibit more robust second or third modes. The large second mode in 306–310 is probably the result of a large, thermocline eddy at this site, seen more clearly in Fig. 4.

A WKB scaling has been applied to both the temporal and the spatial series. After the subinertial profile is removed, the resulting internal-wave profiles are scaled in amplitude and the independent variable—pressure or depth. Removal of the subinertial flow is achieved by either the rotary decomposition of a time series or the subtraction of spatially separated drops. The WKB procedure (Leaman and Sanford, 1975) uses the local Brunt-Väisälä frequency, $N(z)$, to normalize wave amplitude by dividing by $[N(z)/N_o]^{1/2}$ and to stretch (shrink) the vertical scale in proportion to $N(z)/N_o$. A value of 3 cph is taken for $N_o$ throughout this paper, although different $N$ profiles were used for each data set since the observations were taken at different locations and seasons. An example of the Brunt-Väisälä profile and the actual stretched coordinate transformation diagram for the MODE data are shown in Figs. 7a and 7b. The WKB stretching and normalization are discussed further in Appendix B.

The inertial, high-frequency, and raw profiles minus the time-mean profiles (i.e., the total internal wave band) are WKB stretched and normalized, denoted by s and n, according to the procedure of Leaman and Sanford (1975). The resulting profiles are about 1800 sdbars long (Fig. 7) with velocity values every 10 sdbars [pressure in decibars (dbars) and depth in meters (m) or stretched meters (sm) are used interchangeably in this paper]. Short gaps in the original data are closed by linear interpolation. For spectral computations, 160 data points are used, which excludes about 200 m at the top and bottom of the water column.
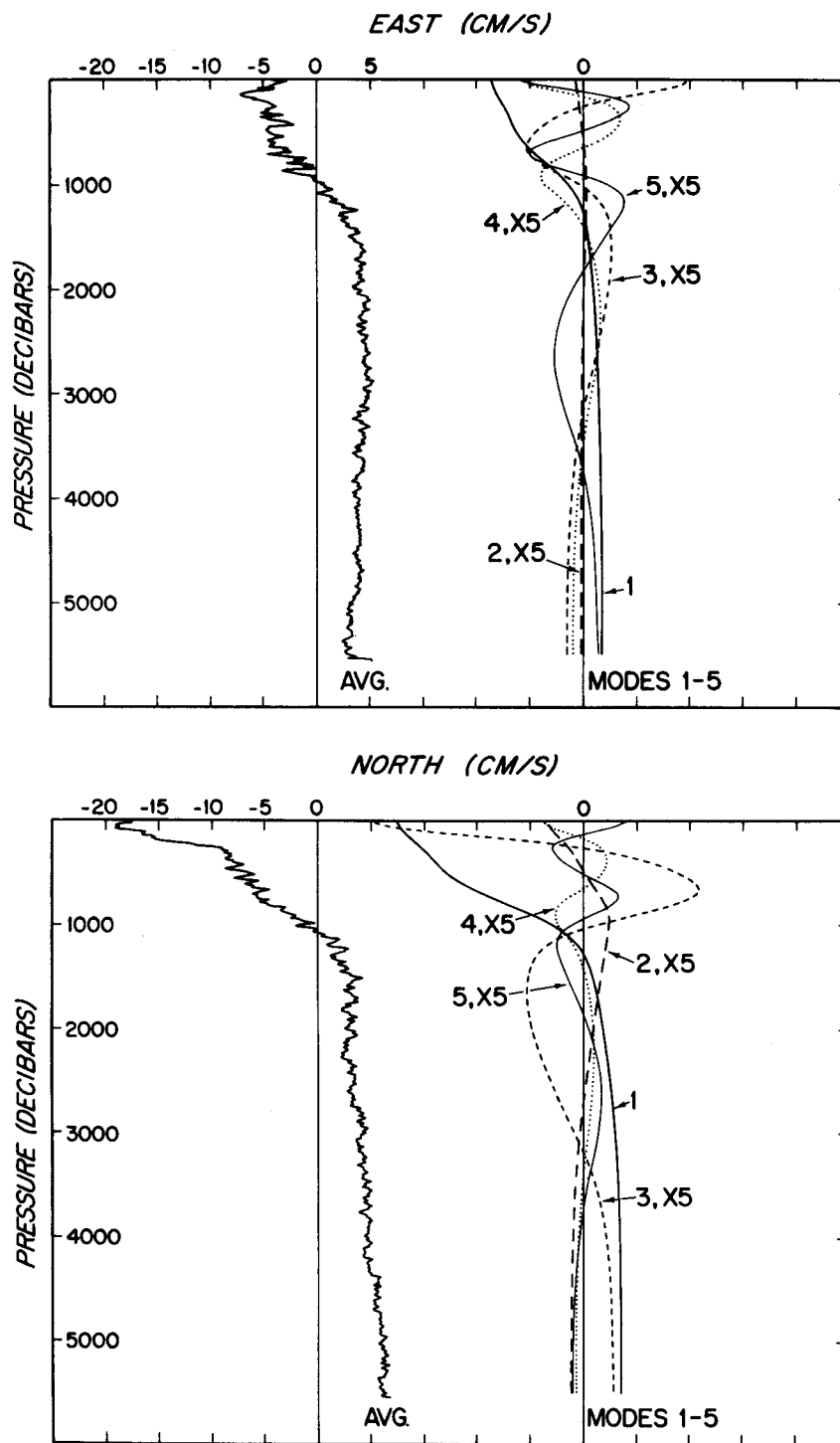
Fig. 3. The first five, flat-bottom, normal-mode amplitudes for the steady velocity profile of Fig. 2. Mode 1 is dominant in both velocity components, while mode 3 is needed to account for the shear above 300 dbars. Modes above the first are plotted at five times their values.
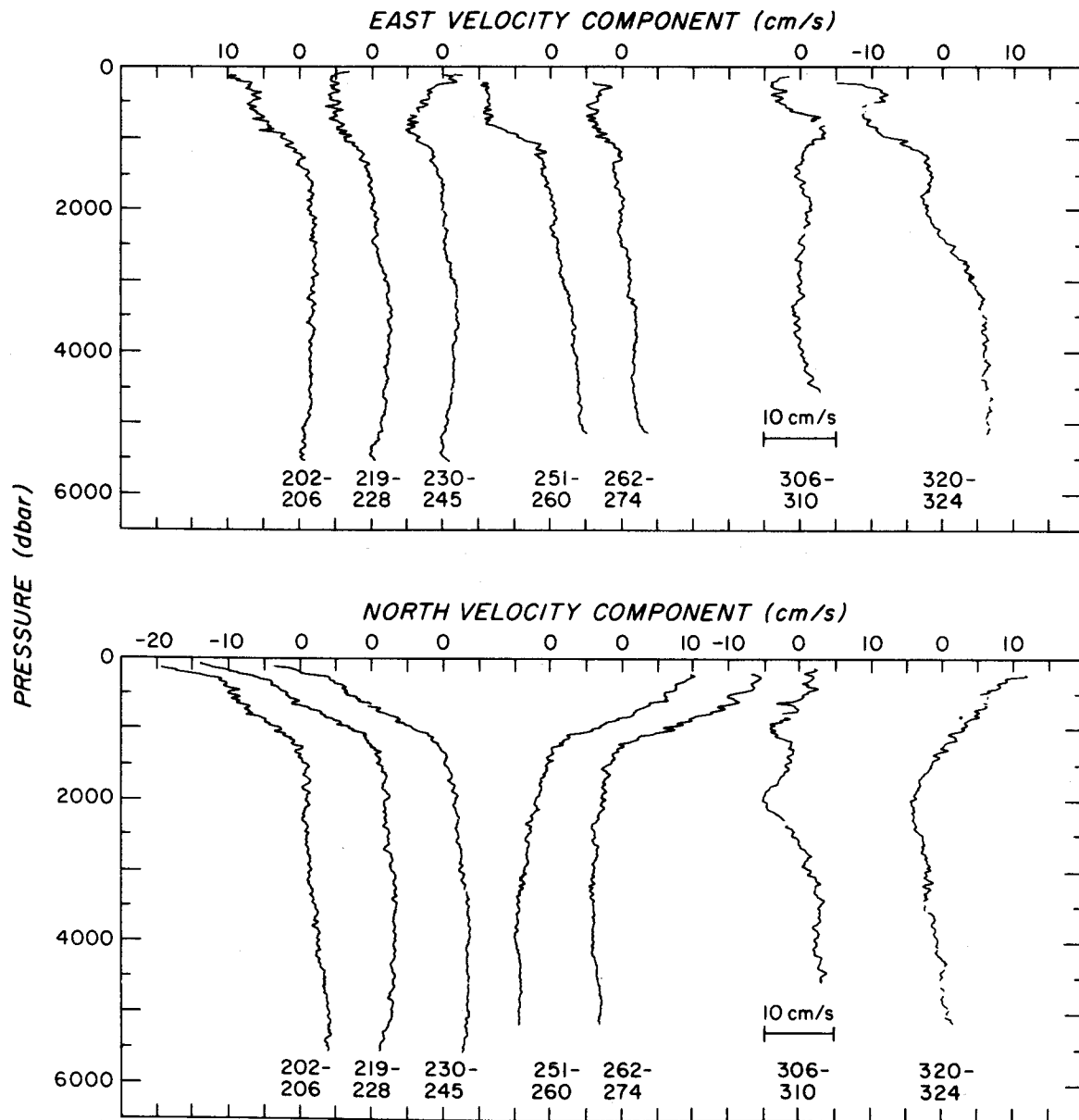
Fig. 4.   Steady velocity profiles for seven time series. The numbers under each profile
correspond to the first and last drop used in each series.


## 4.  THE VERTICAL STRUCTURE OF INTERNAL WAVES

The internal wave profiles were subjected to Fourier analysis. Although velocity values
from nearly the whole water column are used, the vertical wavelengths do not correspond to
modes. First, neglect of the upper 200 m biases the computations; second, only the even modes
correspond to spectral estimates (the odd modes are not individually resolved). This situation
occurs because the modal eigenfunctions are similar to $\cos n\pi Z/H$ whereas the Fourier represen-
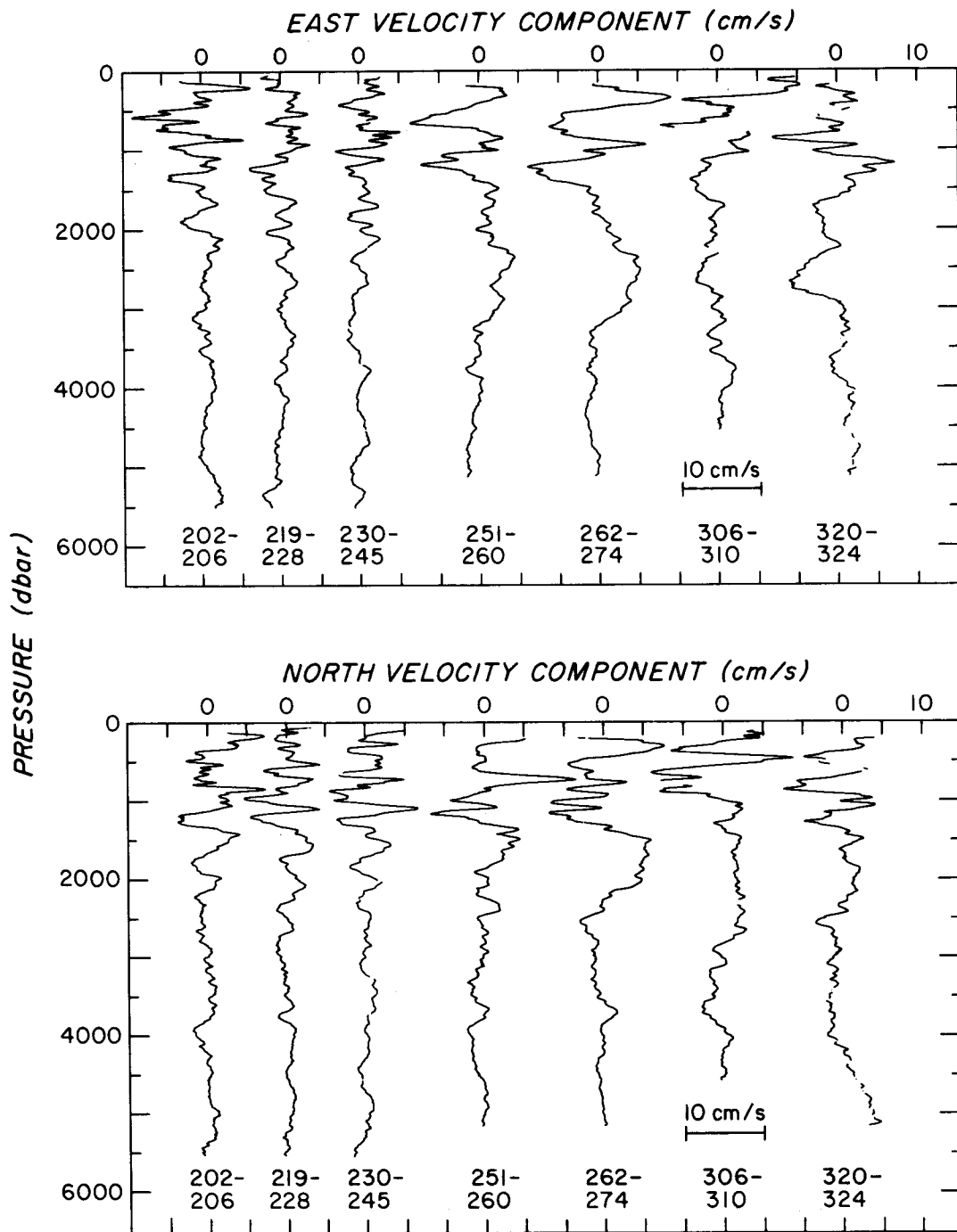
117

Fig. 5. Inertial profiles for the same seven time series used for Fig. 4.

tation uses sin $2n\pi Z/H$ and cos $2n\pi Z/H$. No band averaging is done on the spectra; ensemble averaging is performed over the six inertial determinations and 100 higher-frequency internal wave profiles. It is clear from the visual similarity of adjacent inertial fits that these data are not independent realizations. Because there are three separate groups of profiles, it is assumed that
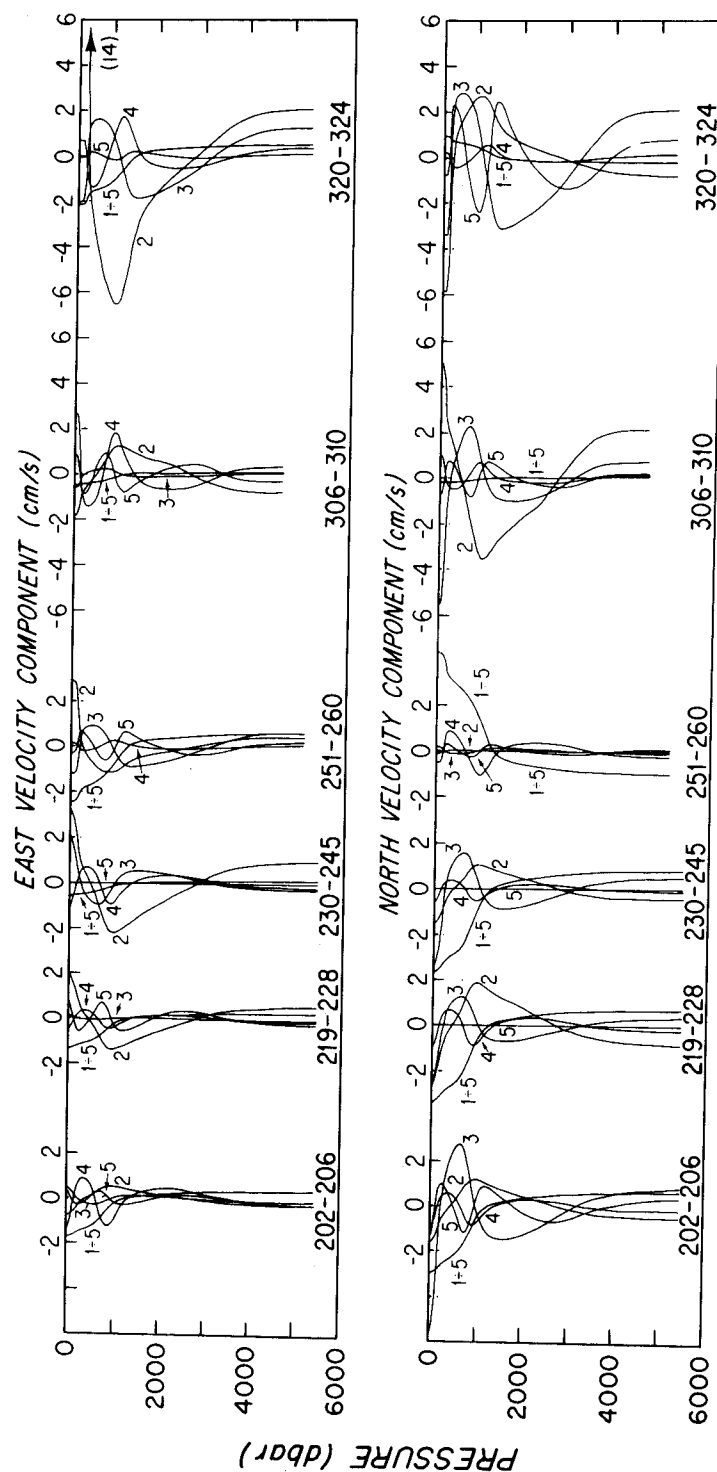
Fig. 6. Modal fits for six profile time series. Fits are made separately for the east and north velocity components. The contributions to the "steady" profile are shown in correct amplitudes for modes 2–5. Mode 1, the dominant one, is shown at 20% of its computed amplitude.
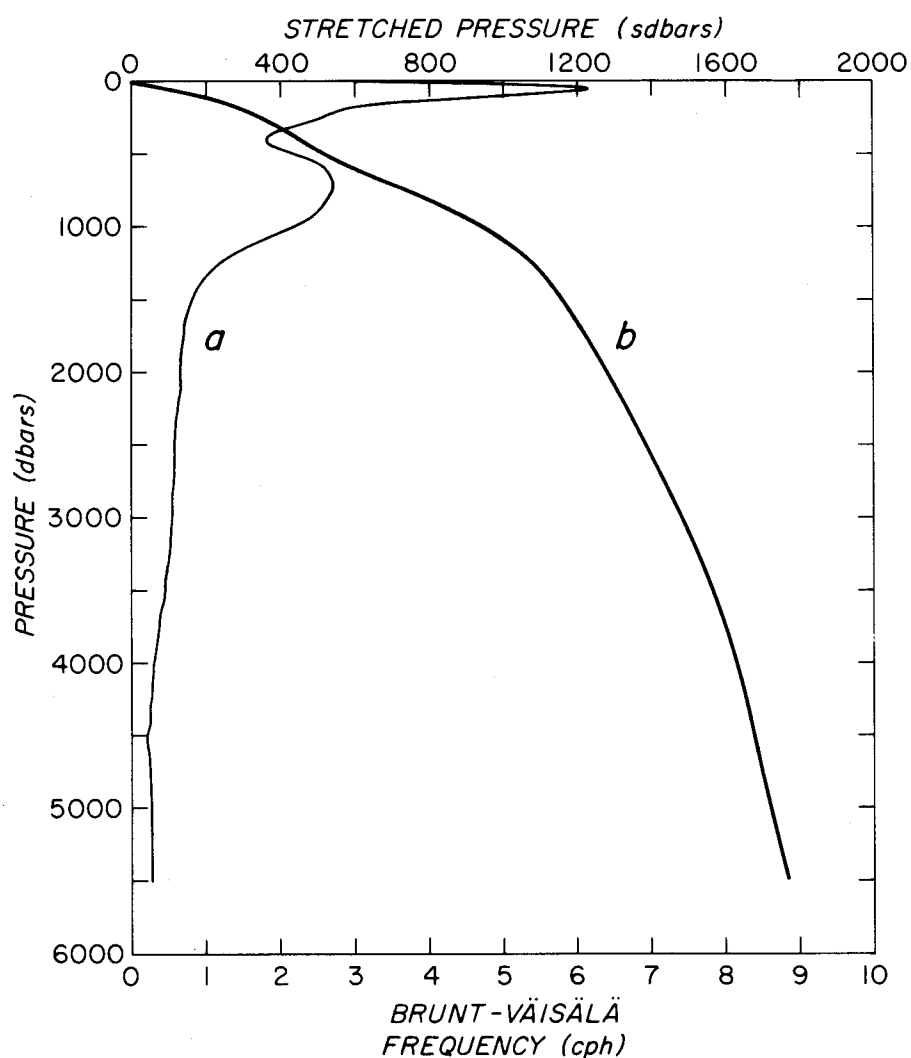
Fig. 7. Brunt-Väisälä frequency profile (line a) at the MODE-I mooring site and relationship of stretched pressure to measured pressure (line b).

these are independent and that the true confidence intervals are at least not larger than those based on two to three realizations. For the high-frequency profiles, down and up profiles are not independent in the deep water, but adjacent profiles taken every 4–7 hours are independent, except insofar as these waves are influenced by common environmental factors such as mean vertical shear or weather. For purposes of statistical inference, it is assumed that the set consists of 50 independent profiles, allowing for some common features on down and subsequent up profiles in deep water.

There are no significant differences between the energy in the east and north components. The separate contributions to the kinetic energy spectrum are shown in Fig. 8 for the original data minus the time-mean profiles. Equipartition between the velocity components is expected (Garrett and Munk, 1972) and observed (IWEX; Müller *et al.*, 1978). These results do not rule out nonequipartition over short portions of the water column or near sources and topography (Johnson and Sanford, 1980; Gordon, 1978).

Only at the lowest wavenumbers is the spectrum consistent with the top-hat dependence of the first GM model (Garrett and Munk, 1972). The spectral slope tends to be flat over estimates 1, 2, and 3 (1600, 800, and 533 sm) followed by a slope of −2 until at a wavelength of about 50 sm and smaller; the high wavenumber slope is about −2.5. The corresponding shear spectrum has a slope between zero and −0.5. The slope is probably not significantly nonwhite and basically agrees with the proposed shear spectrum of Gargett *et al.* (1981).

There is a clear difference in the spectral slope between the inertial and higher-frequency waves (Fig. 9). At vertical wavelengths of about 100 m and longer, the inertial motions are
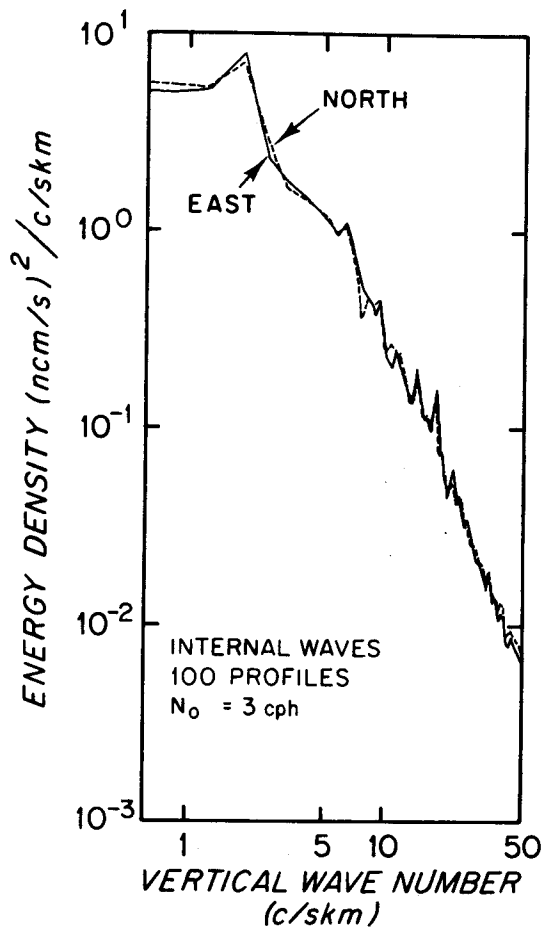
Fig. 8. Energy density spectra in stretched and normalized form for all 100 internal wave profiles for east and north velocity components. The spectrum of kinetic energy would be one-half the sum of the east and north contributions.
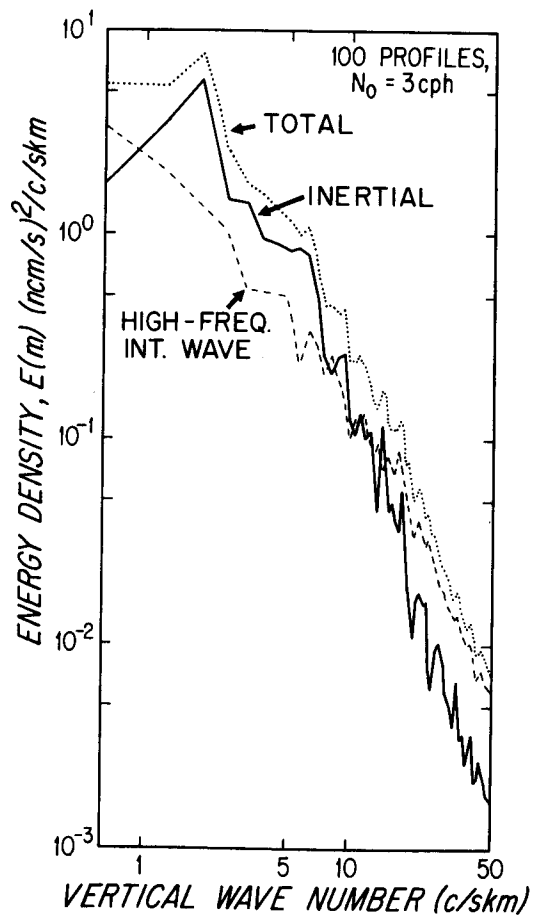
Fig. 9. Kinetic energy density spectra for total internal wave field, the inertial wave contribution, and the high-frequency internal waves. The ordinate is kinetic energy and is one-half the sum of the east and north velocity components.

121

dominant, except for the longest vertical scale, at which they are (or may be) inferior. At all wavelengths shorter than about 100 m, the higher-frequency waves are more energetic. Over the high-wavenumber region (say 5 c/skm and larger), the spectra slopes are about −3 for the inertial and −2 for the HF waves. In both cases the slope depends on the interval over which the fit is made. For example, around 20 c/skm (50 m), there is a slight bump (energy excess) to both spectra which, if heavily weighted in the fit, would force higher slopes to be obtained. Excluding this bump, at the highest wavenumbers (> 20 c/skm) the spectral slopes approach −2.5 for the inertial component and −2.0 for the high-frequency waves.

Other spectral slope determinations have largely resulted from temperature observations. Hayes (1975) reports a slope of −2.5 based on temperature profiles from a CTD; Cairns and Williams (1976) derive a slope of −2 from a drifting, vertically moving temperature sensor, as does Gregg (1977) from his free-fall temperature profiler. The temperature field is relatively unenergetic near $f$ because the motions have little vertical velocity but maximum horizontal kinetic energy. Thus temperature spectra are lacking the lower frequency (and lower wavenumber), energetic inertial signatures. Also, it may be that vertical detrending of temperature profiles (to reduce the contribution from the time-mean temperature field) removes much of the longer vertical wavelength components.

The conventional and rotary spectra (Leaman and Sanford, 1975) of these data are presented in Fig. 10 in the energy-preserving form. The low wavenumber energy cutoff is clearly revealed in panel A beyond a wavelength of about 500 sm. The peak at 2 c/skm is very pronounced, showing that 500 m is a dominant vertical wavelength. There is a secondary peak around 5–6 c/skm, near the third harmonic of the main peak. The inertial energy is principally contained between wavelengths of 150 and 500 sm. At both the lowest and highest wavenumbers, the high-frequency internal waves are more energetic than the inertial motions.

A similar result was reported by Müller et al. (1978) who found during the IWEX experiment that there was little energy in the first three inertial modes (estimates 1 and 2 here), and that most of the energy at these vertical wavelengths was contributed by higher-frequency internal waves. Perkins (1970) found that the third vertical mode was the dominant one in the Mediterranean. The global wave functions of Munk and Phillips (1968) and Fu (1981) have turning latitudes which decrease with vertical mode number. Near-inertial waves will be reflected (attenuated) in a manner inversely related to vertical mode number as they propagate northward. Thus, the observed near-inertial wave field would be deficient of the lowest modes unless these modes were locally forced.

Panels B and C of Fig. 10 show the rotary decompositions of the inertial and high-frequency components. As has been reported by many investigators (e.g., Leaman, 1976; Kundu, 1976), the clockwise rotating (with respect to depth, looking downward) contributions are more energetic. The ascendency of the CW over the ACW is clear in these data, but was not observed in IWEX data (Müller et al., 1978) from a mooring in the MODE-1 area based on calculations of the vertical component of velocity from temperature measurements. It is likely that the IWEX observations contain excessive noise from temperature finestructure.

These are the first abyssal vertical spectra of frequency-separated contributions; previous profile results were based on the whole frequency spectrum (Leaman, 1976), used inertial decomposition over only a short vertical interval and applied no WKB adjustments (Rossby and

Sanford, 1976), or were of thermocline motions (Pinkel, 1981, 1985).

The peak near 2 c/skm in the inertial period energy stands out in the CW component and is missing in the ACW. The CW contribution exceeds the ACW at all vertical wavelengths down to about 100 m. The ACW part is more regular in its wavenumber behavior, while the CW may have some harmonic structure as previously mentioned. It is evident that the ACW inertial component is similar in energy and spectral form to that of the higher-frequency internal waves.

Clearly, CW polarized waves dominate over ACW ones, and this demonstrates that most of the energy is associated with a downward group velocity (CW). The direction of energy flux, on the other hand, is not easily determined from these data. There is insufficient frequency (or, equivalently, spatial) information to calculate the group velocities associated with the upward- and downward-going waves. Near the inertial frequency, the vertical group velocity is

$$Cg = -\frac{(\omega^2 - f^2)}{f\,m} .$$

(3)

The convention is that $m > 0$ corresponds to CW polarized waves and $m < 0$ to ACW waves. The inertial decomposition is not selective enough in frequency to allow $\omega$ to be determined separately for the CW and ACW contributions. In fact, it would take a 100-day-long time series
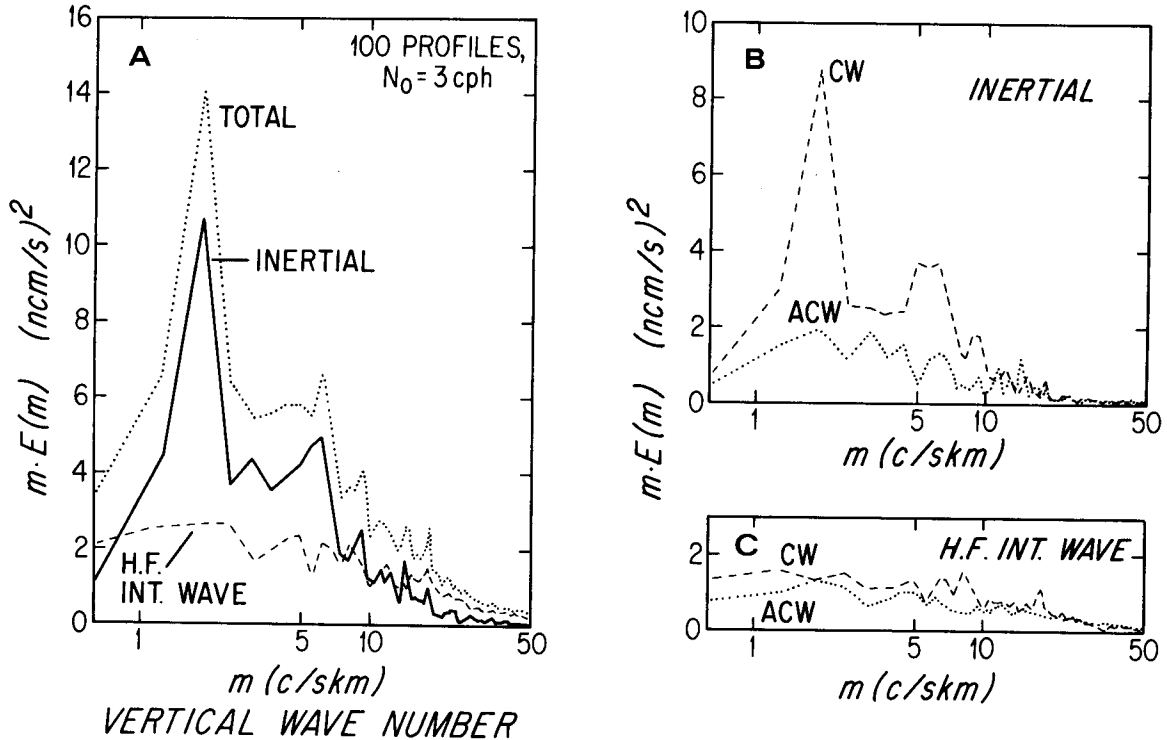


Fig. 10. A: Spectra of Fig. 9 expressed in energy preserving form. B: Inertial component separated into CW and ACW depth-polarized components. C. High-frequency internal waves expressed as CW and ACW spectra.

to get the resolution to about 1% of $f$. Spatial information, however, is readily used to resolve small differences in $Cg$, which can be written for $\omega^2 \ll N^2$ as

$$Cg \doteq -\frac{N^2 k^2}{f\,m^3}, \tag{4}$$

where $N$ is the Brunt-Väisälä frequency and $k$ is the modulus of the horizontal wavenumber associated with the energy at the vertical wavenumber $m$.

In panel C of Fig. 10, the CW and ACW spectra are shown for the high-frequency internal waves. The energies are about equal, demonstrating the vertical symmetry of these waves. Models generally hypothesize vertical symmetry (e.g., Garrett and Munk, 1975), and wave interactions predict equipartition (McComas and Bretherton, 1977).

A check of the WKB scaling results from comparing the upper half of the stretched water column ($\approx 200$–$1000$ dbars of real ocean) with the lower half ($1000$–$5000$ dbars). Such a comparison is shown in Fig. 11. Although the energy levels are not greatly different, demonstrating the usefulness of energy scaling, the vertical wavenumber spectra are systematically and increasingly different at the high-wavenumber end. Several explanations for this discrepancy occur. One is that the WKB scaling amplifies noise in the lower half relative to the upper half. To a first approximation, the measurement noise is essentially the same throughout the water column, so one might expect that the WKB scaling should boost the lower-half noise relative to that in the upper ocean. In Appendix B it is shown that this effect is compensated for by the adaptive filtering, the use of more data in the deep water. Thus the discrepancy probably results from more complex, non-WKB effects or structural changes in the ocean.

The upper-half versus lower-half spectra are presented in Figs. 12 and 13 for the inertial and high-frequency waves. The behavior of the two classes of motion is different; the deeper inertial motions seem more energetic by a factor of about 2 at all vertical wavenumbers, whereas the upper HF waves are more energetic until beyond 10 c/skm, where the spectrum drops rapidly. A high wavenumber cutoff in this range has been reported by Pinkel (1984, 1985) in his upper ocean profiles. The cutoff is not seen in the lower half of the ocean. Another possibility is that the lower half exhibits the results of energy flux from low wavenumbers to high wavenumbers as might be expected from the "whitening" effect of bottom scattering (Eriksen, 1985; Rubenstein, 1988).

The nearly constant ratio between upper- and lower-half inertial-energy densities suggests a wavenumber-independent factor. It is necessary to work with more complete WKB expressions (Phillips, 1977) for horizontal kinetic energy $E$ and vertical wavenumbers $m$:

$$E \propto \frac{(1 + f^2/\omega^2)\,(N^2 - f^2)}{(\omega^2 - f^2)^{3/2}\,(N^2 - \omega^2)^{1/2}}, \tag{5}$$

and

$$m \propto \frac{(N^2 - \omega^2)^{1/2}\,k}{(\omega^2 - f^2)^{1/2}}. \tag{6}$$

For $\omega \sim f$ it is clear that $E$ normalized by $N$ and divided by the vertical wavenumber resolution (to yield spectral energy density) is
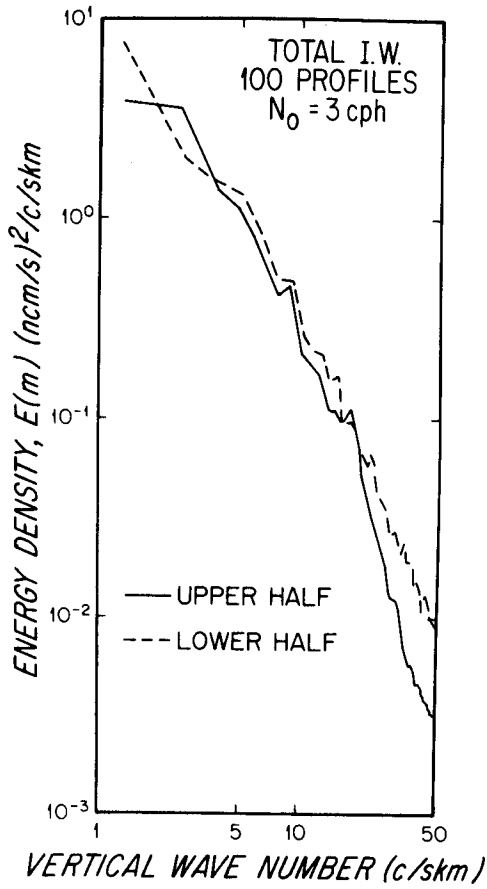
Fig. 11. Kinetic energy density spectra of total internal wave field separated into upper and lower halves of the WKB-stretched water column.
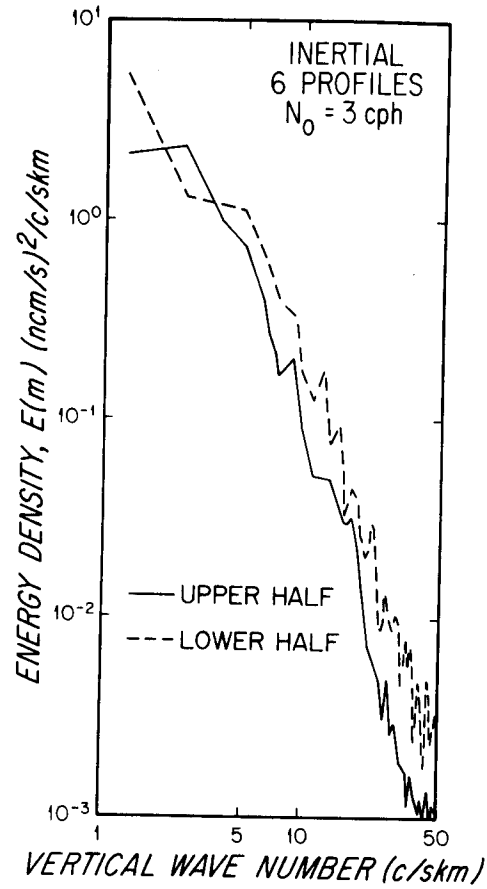
Fig. 12. Kinetic energy density spectra of inertial wave field separated into upper and lower halves of the WKB-stretched water column.

$$\frac{E^*}{\delta m^*} = \frac{E/N}{\delta m/N} = \text{normalized energy density} \propto \frac{1}{(\omega^2 - f^2)} , \qquad (7)$$

with

$$m^* = m/N \propto \frac{1}{(\omega^2 - f^2)^{1/2}} . \qquad (8)$$

Possibly the discrepancy in Fig. 12 results from incorrect $N$ profiles or real departures from WKB scaling. As discussed in Appendix B, the normalized and stretched energy density is independent of $N$ such that it does not change in value if an incorrect $N$ profile is used. The wavenumber scale does change in this case, resulting in a lateral shift of the spectrum. It is not possible for $N$ to be wrong by a factor of 1.5–2, but it does seem likely that the kinematic changes predicted by the WKB expressions are not in equilibrium. That is, the downward-propagating inertial waves, the existence of which is demonstrated by the rotary spectra, must

125

HF.I.W.
100 PROFILES
$N_0 = 3$ cph

——UPPER HALF
- - -LOWER HALF

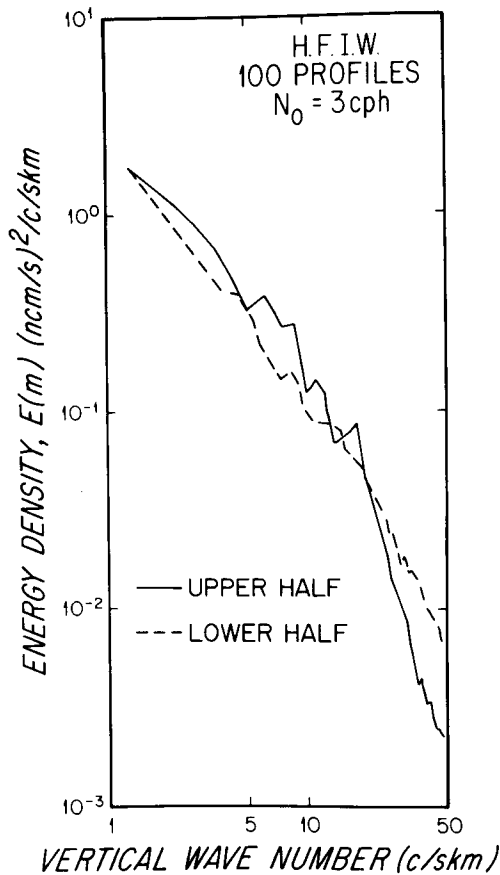ENERGY DENSITY, $E(m)$ $(ncm/s)^2/c/skm$

VERTICAL WAVE NUMBER $(c/skm)$

Fig. 13. Kinetic energy density spectra of high-frequency internal waves separated into upper and lower halves of the WKB-stretched water column. Data gaps result when one or the other profiler experienced noise or loss of data because of tape recorder malfunctions. Table 2 presents the WKB-normalized KE for each spaced pair.

continually undergo structural changes as they go deeper into the lower $N$ region. Thus, there might be a tendency for the wave structure to reflect that of a wave in equilibrium with a slightly higher-than-local value of $N$. Hence, in the deep water, it is reasonable to expect energy that should be at a certain WKB-assigned wavenumber to appear at a *higher* one, since $N$ is essentially monotonically decreasing below the thermocline.

Another possibility is that, if $\omega^2 - f^2$ were smaller in the lower half compared with above, the observed spectral shift in Fig. 12 would occur. That is, as a wave propagates into the deep water, $\omega^2 - f^2$ decreases (by processes to be discussed later), and the WKB-scaled energy (using only $N$) increases and appears at a larger stretched wavenumber. A spectral value will move along the line of slope +2 in the log $E^*/\delta m^*$ vs log $m^*$ plane as $\omega$ changes near $f$. This will occur at all wavenumbers, resulting in a constant offset on the log/log plots of Fig. 12.

A possible mechanism for an $\omega \rightarrow f$ shift in the deep water is the kinematic effects of mean vertical (and, in general, horizontal) shears. In each of the data sets, there was a significant time-mean vertical shear of about 20–40 cm/s over the upper 1000 m. The deep-water shears were much weaker, although if scaled according to Rossby-wave modes (a similar scaling to that used here for internal waves) the shears are comparable to those higher in the water column. To investigate the behavior of near-inertial waves in the presence of vertical shear, it is appropriate to replace $\omega$ by the intrinsic frequency, $\omega - \mathbf{k} \cdot \mathbf{U}(z)$, where $\mathbf{k}$ is the horizontal wavenumber and $\mathbf{U}$ is

126

the time-mean (of frequency $\ll \omega$) horizontal velocity. As near-inertial waves propagate downward from the sea surface, some will experience a frequency shift such that $\omega - \mathbf{k} \cdot \mathbf{U}$ approaches $f$, and the energy density as represented in Eq. (7) greatly increases. Other waves experience the opposite effect and blend into the higher-frequency components. The vertical wavenumber is correspondingly increased, which means that the deep water spectrum is translated along a line of slope = 2, resulting in high energies at every wavenumber. Once below the main shear zone, the refraction ceases, but the waves retain the enhanced energy.

Continuing with this line of speculation, the high-frequency waves also experience shear refraction. The situation here is that, as $N^2 - \omega^2$ becomes small, modifications occur such that horizontal KE density/$N$ becomes larger, while $m/N$ becomes smaller. Explicitly, as $\omega \to N$ in a region of uniform $N$, the expressions are

$$\frac{E^*}{\delta m^*} \propto (N^2 - \omega^2)^{-1} \tag{9}$$

and

$$N^2 - \omega^2 \propto N^4 k^{-2} m^{*2} . \tag{10}$$

Hence,

$$\frac{E^*}{\delta m^*} \propto N^{-4} k^2 m^{*-2} . \tag{11}$$

Thus a point on the spectrum will move along a line of slope equal to –2. For small changes, the spectral distortions would be hard to see, since the data have a slope of about –2.

A second consequence of shear refraction is the possibility of critical layer processes. Internal waves of a given frequency have smaller horizontal phase velocities as the vertical wavenumber is increased. Away from $N$ and $f$, the horizontal phase velocity can be approximated as

$$c = N_o/m^* . \tag{12}$$

Critical layer absorption can occur as the waves propagate through an ambient velocity shear. Let $\delta U$ be the velocity difference between the level of wave generation and the point at which $\delta U = c$ where critical layer processes occur. For a given $\delta U$ over the domain of interest, waves of vertical wavenumber greater than $m_C^*$ (where $m_C^* = N_o/\delta U$) will experience refraction and critical layer processes. The energy discrepancies seen in Fig. 13 may result from shear refraction and critical layer absorption. A two-part internal wave field is hypothesized by Munk (1981). At low vertical wavenumbers ($m^* < m_C^*$), the energetic, *intrinsic* waves occur, while at smaller scales ($m^* > m_C^*$), there are *compliant* waves which are greatly modified by interactions with the intrinsic field.

The change in slope in Fig. 13 occurs at a wavelength of 50 sm. The corresponding velocity difference, $\delta U$, is 5 cm/s, a value not frequently observed over 50 sm in the time-mean flow but one common to the inertial motions. The shear over 50 sm is taken to be caused by an inertial wave with a vertical wavelength of 200–300 sm.

## 5. THE HORIZONTAL STRUCTURE OF INTERNAL WAVES

Certainly the most unexplored aspect of internal waves is their horizontal structure. To a limited extent, IWEX (Briscoe, 1975; Müller et al., 1978) described the horizontal wavenumber dependence of internal waves. Much more extensive observations have been reported by Katz (1975) using towed sensors, Stegen et al. (1975) from XBT patterns, and Pinkel (1975) using a spaced array of temperature profilers and, later, horizontally directed Doppler sonar. There are a few, but widely divergent, estimates of the horizontal wavelengths of near-inertial waves based on moored current meters (Webster, 1968; Fu, 1981; Pollard, 1980). More recent observations with XCPs by D'Asaro (1984) have revealed spatial coherence scales of internal waves in the upper ocean. The data set presented here is a small but unique one demonstrating a clear pattern to the horizontal dependence of internal waves.

The original intention was to compare these observations with the expectations of Garrett and Munk (1975) expressed in their dropped horizontal coherence (DHC). The pursuit of DHC calculations was suspended because the data set was too small to yield reliable estimates. More-over, interpolation was necessary across the data gaps before WKB vertical stretching was applied. Thus it was decided that the vertical wavenumber and horizontal dependence of DHC could not be adequately tested with the present data.

Rather than the DHC calculations, the mean square differences between the horizontally spaced profiles are computed. This quantity is identical to a structure function of zero depth lag. The KE estimates are based only over depth intervals in which *both* profiles are good; there are gaps in the difference profiles wherever either profile was missing data. Measurements from the surface to 5550 dbars, every 10 dbars, are used for 556 possible velocity differences. The velocity differences are normalized by $[N_o/N(z)]^{1/2}$, the WKB amplitude scaling.

A set of profile differences, before WKB scaling, is shown in Fig. 14. There is a clear progression toward larger $\Delta X$. Also, the dominant vertical scale increases with $\Delta X$, consistent with the dispersion relationship between vertical and horizontal wavelengths for inertial-period internal waves.

An attempt has been made to demonstrate the dominance of the inertial energy at the $\Delta X = 12.5$ km separation. The inertial fit was computed for the MODE-I center time-series drops 236 through 245. This fit was then rotated in time to the time of the 241/242 drop pair. The rotated fit and the difference profiles are presented in Fig. 15. There is substantial agreement throughout the water column, although the correspondence is clearly better below the thermocline (1000 m). The correspondence may be improved by rotating the inertial fit slightly, but the present example serves to demonstrate the presence of inertial waves in the velocity differences. Incidentally, the superior agreement below 1000 m may add credibility to the argument in the previous section about $\omega^2 - f^2$ being smaller (and, possibly, more narrow band) in the deep water than in the upper ocean.

Table 2 presents the normalized variances of the difference profiles. At the smaller horizontal separation, the normalized kinetic energy is 2.5 ncm$^2$/s$^2$. Since the depth-averaged N is 1 cph, the average kinetic energy of the difference profile is about 0.8 cm$^2$/s$^2$. There is a steady trend toward higher kinetic energies at larger horizontal separations, culminating in about an order-of-magnitude-larger value at 12.5 km. The mean square differences between the two EM sensors (for redundancy, there is a pair of EM sensors on each profiler) are on average less than
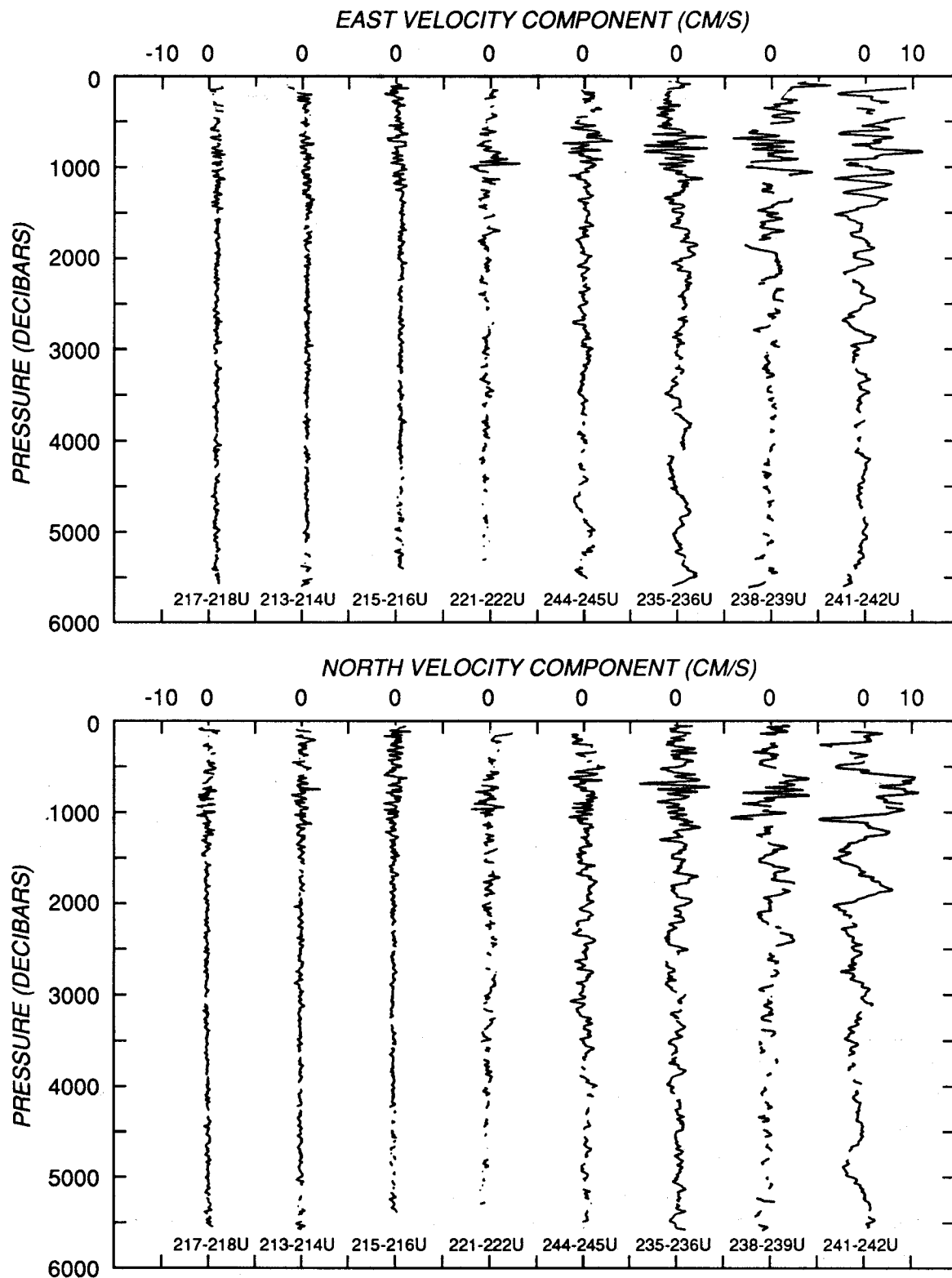
Fig. 14.  Profiles of the differences in velocity components for pairs of simultaneous drops. The numbers beneath each profile represent the drop numbers of the pair, and the letters denote use of either the down (D) or up (U) portion of the profiles.
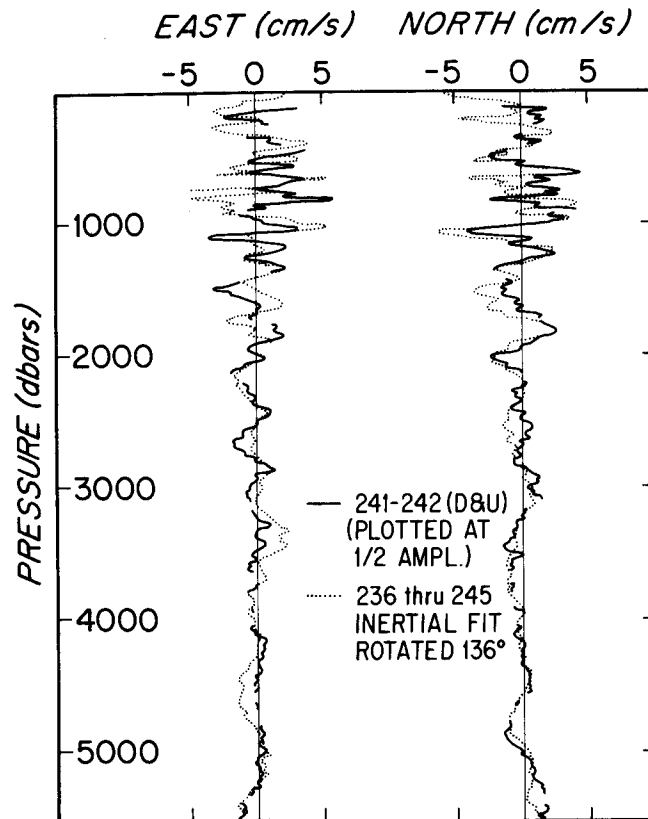
Fig. 15.  Difference profile for drops 241 and 242 (down and up portions averaged) plotted at half amplitude (a value chosen to increase visual comparison) versus the inertial fit of the time series at the central mooring (including drop 242) rotated 136° forward in time from the reference time used for display of fit in Fig. 5.

0.5 ncm$^2$/s$^2$, which suggests that much of the interprofiler variance is due to apparent velocity differences induced by depth (pressure) errors acting on a shear field. That is, it is thought that most of the variance in profile differences at small $\Delta X$ originates from systematic pressure errors between the profilers. A pressure offset shifts one profile vertically with respect to the other, resulting in apparent velocity differences when small vertical-scale shear is present.

The background internal-wave energy has been computed over the MODE center profiles minus a time-mean profile. The time-mean profile was constructed from all MODE center profiles from drop 235 through drop 245, the profiles constituting the largest horizontal separations and largest energy differences. The residue profiles are considered to be of internal waves and have an average normalized energy of 15.4 ncm$^2$/s$^2$. Thus the difference profiles at $\Delta X$ = 6.7 km contain a kinetic energy level about equal to that in the internal-wave background field.

Table 2. A summary of WKBJ normalized horizontal kinetic energy of difference profiles. The average N over the water column is 1 cph, and the value of $N_o$ is 3 cph.

| Profiles | Separation (km) | % good of 556 pts | ΔKE (ncm/s) |
|---|---|---|---|
| 217-218D | 0.015 | 96 | 1.8 |
| 217-218U | 0.015 | 89 | 2.1<br>2.3 |
| 213-214D | 0.05 | 89 | 2.4 |
| 213-214U | 0.05 | 87 | 2.4<br>2.3 |
| 215-216D | 0.1 | 42 | 2.7 |
| 215-216U | 0.1 | 83 | 2.5<br>2.3 |
| 221-222D | 0.4 | 37 | 2.6 |
| 221-222U | 0.4 | 55 | 2.9<br>3.1 |
| 244-245D | 1.5 | 60 | 4.7 |
| 244-245U | 1.5 | 82 | 5.1<br>5.5 |
| 235-236D | 4.8 | 76 | 11.1 |
| 235-236U | 4.8 | 94 | 11.1<br>11.0 |
| 238-239D | 6.7 | 47 | 14.6 |
| 238-239U | 6.7 | 64 | 14.3<br>14.0 |
| 341-242D | 12.5 | 86 | 23.2 |
| 341-242U | 12.5 | 93 | 23.6<br>23.9 |

The results shown in Table 2 are plotted in Fig. 16. The solid line is a fit to the data with an intercept of 2.5 $ncm^2/s^2$, which is taken to be the noise level common to measurements at all separations. The dashed line has the same slope as the solid line but with the additive noise removed.
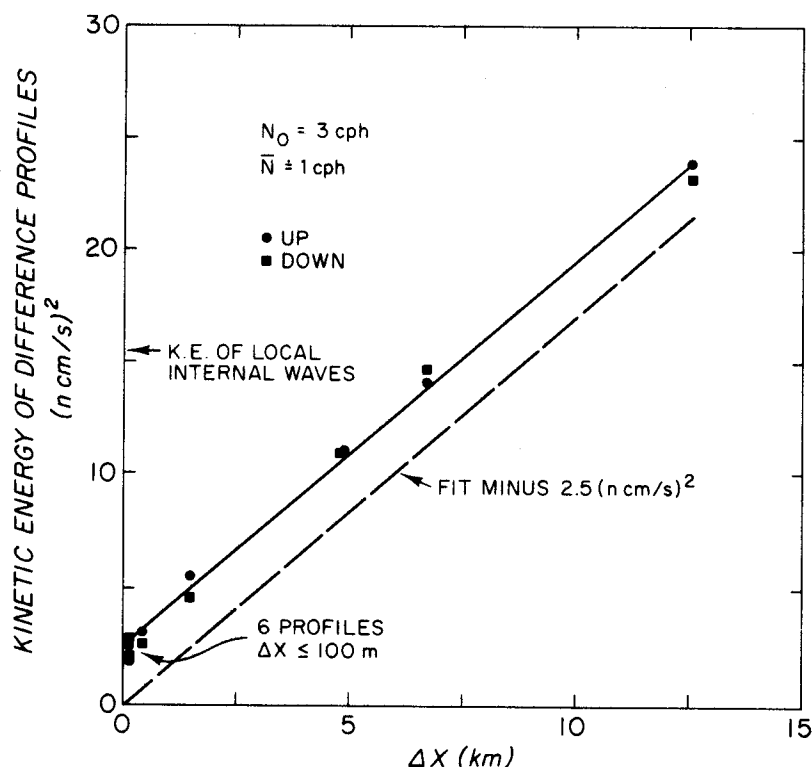
Fig. 16. Kinetic energy of the difference profiles for simultaneous pairs of Fig. 15 in normalized energy units. Both down and up portions of profile pairs are shown. If the energy of difference pairs at a small separation is uncorrelated noise, the fit can be reduced by this noise (about 2.5 n cm/s), and the result is shown as a dashed line. One way to view these data is to recognize that the profiles have zero correlation when the kinetic energy of the difference profiles exceeds the average kinetic energy of the local internal wave field (15 (n cm/s)$^2$).

The cross-structure function can be expressed in terms of correlation functions and the internal-wave energy in each profile going into the pair. Let $u_1$, $v_1$ represent profile 1 of a pair and $u_2$, $v_2$ represent the other profile. Then

$$KE \text{ of } \Delta \underline{v} = \frac{1}{2} \left[ \overline{(u_1 - u_2)^2} + \overline{(v_1 - v_2)^2} \right],$$ (13)

where the overbar represents a vertical average over all (good) data, which for the following is assumed to be the whole water column. The cross correlation function is

$$R_{u_1 u_2} = \frac{\overline{u_1 u_2}}{\left[ \overline{u_1^2} \cdot \overline{u_2^2} \right]^{1/2}},$$ (14)

with a similar expression for $R_{v_1 v_2}$. Assuming the internal wave statistics are spatially uniform, then $\overline{u_1^2} = \overline{u_2^2} \equiv \overline{u^2}$, $\overline{v_1^2} = \overline{v_2^2} \equiv \overline{v^2}$, and $u$ and $v$ are isotropic ($R_{u_1 u_2} = R_{v_1 v_2} \equiv R$); then

$$\frac{1}{2} \overline{|\Delta v|^2} = 2(1 - R) \cdot \frac{1}{2} \overline{v^2}.$$ (15)

The KE of difference profiles should be zero at $\Delta X = 0$, increasing to four times the average KE of v as $R$ goes toward $-1$ (only for single wave) and ultimately approaching two times the average KE of v as $R$ goes to zero for large $\Delta X$. From Fig. 16 it is evident that $\frac{1}{2} |\Delta v|^2 = v^2$ (i.e., $R = 0$) for $\Delta X \sim 15$–20 km. The separations are not large enough to reveal the asymptotic behavior of the difference KE.

The MODE-I eddy does not contribute significantly to the velocity differences presented in Fig. 16. The absence of low-mode eddy structure in the differences of Fig. 15 demonstrates the absence of mesoscale eddy contamination. The MODE-I eddy had a zero correlation scale of 100 km (MODE Group, 1978) and a correlation function of the form

$$R = \cos\frac{\pi \Delta X}{200 \text{ km}} \quad \text{for } \Delta X \ll 100 \text{ km} . \tag{16}$$

The eddy field had a local KE of 25 $(cm/s)^2$, or in normalized units was 75 $ncm^2/s^2$ since $N_o / \overline{N} \doteq 3$. Thus the eddy interference is estimated to be about 1 $ncm^2/s^2$ at $\Delta X = 6.7$ km and 3 $ncm^2/s^2$ at 12.5 km. It may be that the mean square differences at $\Delta X > 15$ km would be strongly influenced by mesoscale contamination. On the other hand, the drops at large $\Delta X$ were aligned parallel with the flow and, hence, normal to the first-order velocity gradient. Moreover, little of the MODE-I eddy structure, primarily first mode, is seen in the velocity differences of Fig. 14.

## 6. CONCLUSIONS

The present study describes the spatial structure of thermocline and abyssal internal waves. Velocity profiles usually span only the upper ocean and are seldom deeper than the base of the main thermocline. WKB normalization and stretching are applied to the velocity components and vertical coordinate, respectively. The WKB-scaled profiles exhibit much more vertical homogeneity and can be used to reveal differences between upper-ocean and abyssal internal-wave characteristics.

The principal conclusions of the analyses of these velocity profiles are

1. East and north contributions to total internal wave kinetic energy are equal as is consistent with statistical isotropy in the horizontal.

2. Bulk of the internal wave energy is contributed by near-inertial motions.

3. Frequency-wavenumber dependence of internal wave spectra is nonseparable: near-inertial motions exhibit a power law $\propto m^{-3}$, whereas higher frequency waves exhibit a power law $\propto m^{-2}$.

4. Near-inertial wave motion is clockwise polarized with depth and is most energetic at 500-m wavelength with lesser energy contributed by the band 100–300 m.

5. High-frequency internal waves exhibit no departures from isotropy, either in the vertical (i.e., polarization) or in the horizontal coordinates.

6. Upper-ocean internal waves exhibit a spectral cutoff in high-vertical wavenumber energy compared with the lower half of the water column, suggesting action by dissipative effects in the upper ocean and/or scattering effects ("whitening") in the abyssal ocean.

7.  A horizontal, spatial correlation scale of 15–20 km existed for the MODE-I internal wave field.

Even the crude frequency separation possible with these short time series reveals the distinctly different spectral slopes for the inertial waves compared with the high-frequency internal waves. Spectral stability is achieved with ensemble averaging, rather than band averaging. As a result, the spectra retain the lowest wavenumber components, including essentially one wavelength over the entire water column.

The near-inertial motions predominate at vertical wavelengths longer than 100–200 m, at which point the high-frequency internal waves become more energetic. These differences may be expressions of wave–wave processes. McComas and Müller (1981a) find that, under conditions of energy or action fluxes governed by the processes of induced diffusion and dissipation, a spectral slope of –2 at all frequencies is not an equilibrium solution in the presence of flux and dissipation. In contrast, power law slopes of –2.5 at inertial and –2.0 at high frequencies are near-equilibrium solutions. The steeper slope for near-inertial motions supports the view that the wave field may be in equilibrium.

These results demonstrate that a separable frequency and vertical wavenumber description of these data is not appropriate. Garrett and Munk (1972, 1975) suggested a spectral model in which the same vertical wavenumber dependence was hypothesized at all frequencies. Clearly, such a model is not supported by these observations. The maverick is the inertial motions; it seems likely that the higher-frequency waves do follow a frequency-independent vertical structure. The inertial contribution, on the other hand, is more distinct owing to spotty generation and its isolation or uniqueness among the internal wave continuum. It seems less interactive and more independent than the rest of the internal waves (McComas and Bretherton, 1977; Olbers, 1983; McComas and Müller, 1981a,b).

At the longest vertical wavelengths, approximately one or two cycles per (normalized) water depth, the CW and ACW energy components of the inertial motions decrease markedly, becoming about equal at the lowest wavenumber. The tendency toward modes or symmetric energy composition is to be expected because of surface and bottom reflections; the decrease in energy for wavelengths greater than 500 sm is not easily understood. Pollard (1970) predicts that mode 1 is most easily forced by surface stress because of its large vertical group velocity. Perhaps the time-mean shear acts to destroy, or dismember, the lowest modes.

The separation of the total internal waves into upper and lower halves revealed mostly a divergence of the spectra of the upper ocean relative to the lower part for wavelengths less than 100 m. The inertial component does not exhibit this behavior; the main characteristic of this component is that the lower half is more energetic at all wavenumbers. The source of the divergence of the spectra is the high-frequency internal waves. At vertical wavelengths shorter than 50 m, the slope of the upper-ocean spectra changes from –2 to –4. One possible cause is the interaction of the internal waves with the time-mean thermocline shear. Bottom scattering should move energy from longer vertical wavelengths to shorter. Hence, the upper half/lower half differences may result from the whitening effects of bottom scattering (Rubenstein, 1988).

The zero-correlation distance of 15–20 km is considerably smaller than previously reported. Earlier measurements have largely been near the sea surface and have observed much longer horizontal scales. For example, Pollard (1980) reported horizontal wavelengths of several hundred

meters in the SML. D'Asaro (1984) observed inertial-wave coherence scales that seemed to decrease with depth, consistent with the present, much deeper results. The increase in variance between profiles obtained up to 12.5 km apart, essentially a structure function, is useful in estimating errors in comparing measurements taken at separated sites, such as profiler and moored current meter comparisons.

Velocity profiles over the entire water column are useful for studies of internal waves. The observed energy levels are lower in the deep ocean than in the thermocline but not after WKB scaling. Deep internal waves exhibit characteristics that should be more nearly in equilibrium since they are more distant from surface sources and thermocline interactions. The spatial structure of internal waves is a sensitive measure of wave frequency through the dispersion relation. Wave period determinations can be obtained from the spatial structure of the dominant internal wave with better resolution than a long time-series of moored observations. It is likely that models for internal wave characteristics would be better tested on subthermocline motions. Abyssal velocity observations are needed to evaluate proposals that abyssal mixing rates and diffusivity are larger than in the upper ocean. Methods are available for more extensive subthermocline observations in support of modern internal wave studies.

## APPENDIX A

In Section 3 it was asserted that the inertial fit produces a profile that is uncorrelated with the residue or higher-frequency profiles. To examine this concept further, consider a simple, two-component model for the internal wave field:

$$u + iv = A \ e^{ift} + B \ e^{i\omega t} \ . \tag{A1}$$

The inertial decomposition is the solution to

$$\frac{1}{T} \int_0^T (A \ e^{ift} + B \ e^{i\omega t} - C \ e^{ift})^2 dt = \text{minimum} , \tag{A2}$$

where the summation over the finite number of profiles has been replaced with an integration over the duration $T$. The solution is

$$C(z) = A(z) + B(z)I , \tag{A3}$$

where

$$I = \frac{1}{T} \int_0^T e^{i(\omega - f)t} dt \ . \tag{A4}$$

The high-frequency internal waves are the total internal wave field minus the inertial fit:

$$u + iv - C \ e^{ift} = B \ (e^{i\omega t} - I \ e^{ift}) . \tag{A5}$$

The energy spectra with respect to vertical wavenumber averaged over all profiles are as follows, where the symbols ^ and * represent a Fourier transform with respect to depth and complex conjugate, respectively.

For the total wave field:

$$\frac{1}{T}\int_o^T \left[\hat{A}^2 + \hat{B}^2 + \hat{A}\hat{B}* \ e^{-1(\omega-f)t} + \hat{A}*\hat{B} \ e^{i(\omega-f)t}\right] dt \qquad (A6)$$

$$= \hat{A}^2 + \hat{B}^2 + \hat{A}\hat{B}*I* + \hat{A}*\hat{B}I \ .$$

For the inertial component:

$$\frac{1}{T}\int_0^T \left[\hat{A}^2 + \hat{B}^2 + \hat{A}\hat{B}* \ e^{-i(\omega-f)t} + \hat{A}*\hat{B} \ e^{i(\omega-f)t}\right] dt \qquad (A7)$$

$$= \hat{A}^2 + \hat{B}^2 I^2 + \hat{A}\hat{B}*I* + \hat{A}*\hat{B}I \ .$$

For the higher-frequency component:

$$= \frac{1}{T}\int_0^T \hat{B}^2 \left[1 - I* \ e^{i(\omega-f)t} - I \ e^{i(\omega-f)t} + I^2\right] dt \qquad (A8)$$

$$= \hat{B}^2(1+I^2 - I*I - II*) \qquad (A9)$$

$$= \hat{B}^2(1-I^2) \ .$$

The sum of the inertial and higher-frequency components is

$$= \hat{A}^2 + \hat{B}^2 + \hat{A}\hat{B}*I* + \hat{A}*\hat{B}I \ . \qquad (A10)$$

Hence, the total energy equals the sum of the parts. In general, for a continuum of internal waves, the spectrum of the total internal wave energy should equal the sum of the inertial and high-frequency waves as here computed.

## APPENDIX B

The WKB scaling and normalization (s & n) involves three steps:

1. Normalization based on a chosen reference Brunt-Väisälä frequency:

$$U_1^*(z) = (N_o/N)^{1/2} \ U(z). \qquad (B1)$$

2. Adaptive filtering in which original observations are averaged over an interval determined by the local value of $N/N_o$:

$$U^*(z) = \frac{N(z)}{N_o \Delta z} \int_{\zeta_1}^{\zeta_2} U_1^*(\zeta) d\zeta, \qquad (B2)$$

where

$\Delta z$ = the data spacing in the original profile (assumed to be uniform).

$\zeta_1$ = $z - N_o \Delta z/2N(z)$

$\zeta_2$ = $z + N_o \Delta z/2N(z)$.

3. Stretching introduces a new depth scale, $z^*$, that is related to the measured depth scale:

$$z^* = \frac{1}{N_o} \int_o^z N(\zeta)\, d\zeta .$$ 

(B3)

Schematically the procedure is shown in Fig. B1.

The horizontal kinetic energy in the s & n series is

$$\frac{1}{2}\left[\overline{U^{*2}} + \overline{V^{*2}}\right] = \frac{1}{2H^*} \int_{-H^*}^{o} \left\{ \left[U^*(z^*)\right]^2 + \left[V^*(z^*)\right]^2 \right\} dz^* .$$ 

(B4)

For now, ignore the effect of the adaptive filter and note that

$$dz^* = \frac{N(z)}{N_o}\, dz ,$$ 

(B5)
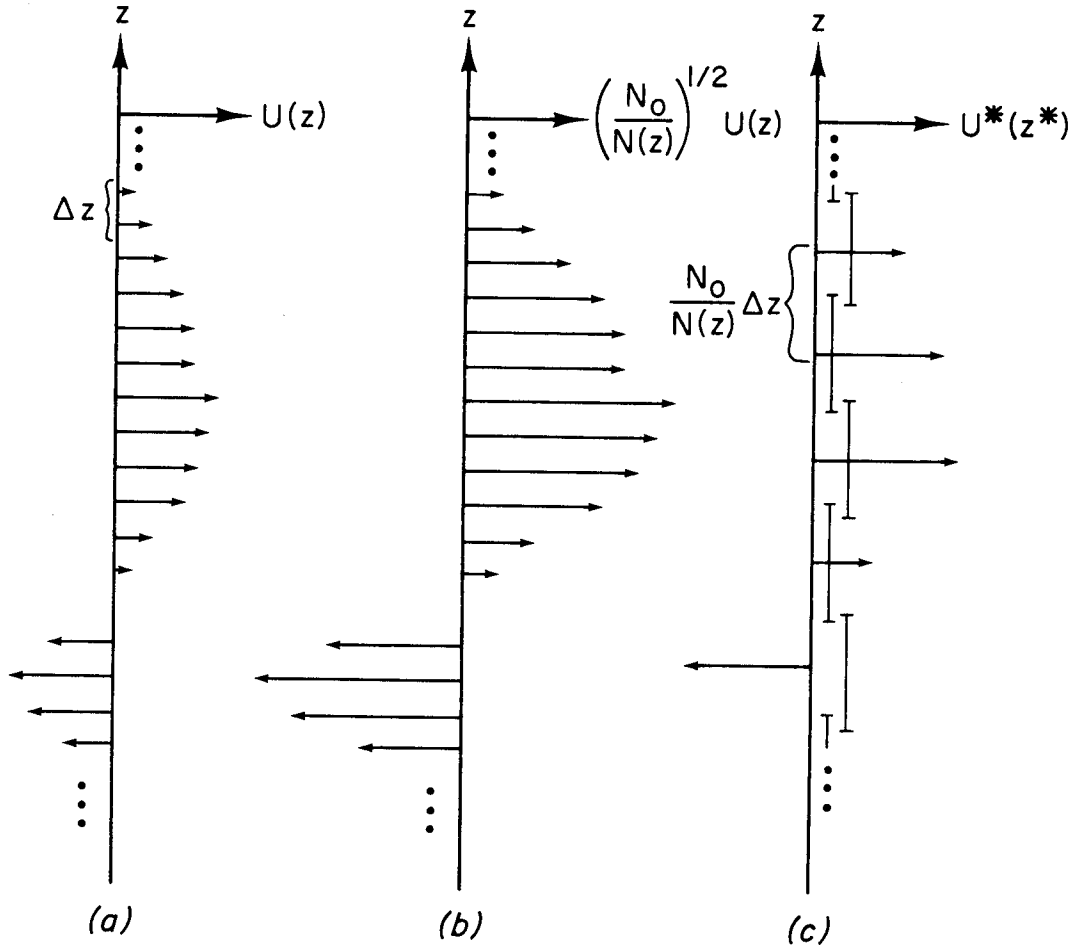


Fig. B1.   (a) Example of a profile of velocity component $U(z)$. (b) The same profile after scaling by $[N_o/N(z)]^{1/2}$. (c) The vertical sampling resulting from WKB stretching of the vertical coordinate.

137

$$\overline{N} = \frac{1}{H} \int_z^o N(\zeta) d\zeta \tag{B6}$$

and

$$H^* = \int_{-H}^o \frac{N(\zeta)}{N_o} d\zeta = \frac{H\overline{N}}{N_o} . \tag{B7}$$

So

$$\frac{1}{H^*} \int_{-H^*}^o [U^*(z^*)]^2 dz^* = \frac{N_o}{H\overline{N}} \int_{-H}^o U^2(z) dz \tag{B8}$$

or

$$\overline{U^{*2}} = \frac{N_o}{\overline{N}} \overline{U^2} , \tag{B9}$$

when no adaptive filtering is used.

In the case in which the $U^*(z^*)$ series is split in two, the upper half $\overline{N} \sim 2$ cph and the lower half $\overline{N} \sim 0.7$ cph. Thus the KE is $N_o/\overline{N} \sim 3$ times larger in the stretched and normalized series than in the original. If the noise, $U_N$, were independent of depth, then

$$\overline{U_{N_{upper}}^2} = 1.5 \overline{U_N^2}$$

and

$$\overline{U_{N_{lower}}^2} = 4.5 \overline{U_N^2} .$$

Hence, an amplification of noise is expected in the lower half relative to the upper. This is what is seen.

However, include now the adaptive filter which averages over measurements with a box-car width proportional to $N_o/N(z)$. The noise variance should decrease in proportion to $N(z)/N_o$ (i.e., inversely to the number of data points taken into the average). The noise contribution is now $[N(z)/N_o] U_N^2$, and the stretched and normalized energy is

$$\overline{U_N^{*2}} = \frac{N_o}{\overline{N}} \overline{\left[ \frac{N}{N_o} U_N^2 \right]} \sim \overline{U_N^2} . \tag{B10}$$

Therefore, no amplification of noise is expected.

According to Sanford et al. (1978) the difference between simultaneous velocity profiles by two EMVP instruments is less than 0.7 cm/s rms. The noise variance is then $\sim 0.5$ (cm/s)$^2$ If it is considered as spectrally white and due to equal contributions from each instrument, then

$$E(m) = \frac{0.5 \text{ (cm/s)}^2}{50 \text{ cpkm}} \cdot 1/2 = 5 \cdot 10^{-3} \text{ (cm/s)}^2/\text{cpkm} .$$

This variance should be independent of depth and comparable to that seen on the upper half versus the lower half spectra of Fig. 11. That is, the difference between the curves of Fig. 11 could be explained by larger noise in the deep water.

This analysis suggests that the differences between the upper and lower half may be real but they are close to the noise level, although there is no expectation for more noise in the lower half than in the upper.

With the WKB scaling and normalization, the horizontal kinetic energy *density* estimates are independent of $N$. The KE density is $|\hat{U}^*(m^*)|^2/\delta m^*$ where $\hat{}$ represents the Fourier transform and $\delta m^*$ is the wavenumber resolution, i.e., $2\pi/H^*$. Since $U^* = (N_o/N)^{1/2}U$ and $\delta m^* = N_o \delta m/N$, and under the WKB assumption variations in $N$ are small compared with those of $U$ at any $m$, then $\hat{U}^{*2}/\delta m^* = \hat{U}^2/\delta m$. Therefore, spectral density estimates are invariant to $N$ but are shifted by WKB scaling and normalization with respect to $m$. For example, suppose the wrong value of $N$ was used for some profiles. The values of energy density will not be incorrect, but the wavenumbers will be. Hence, if there was a strong single wave in all velocity profiles, the use of a wrong $N$ profile would result in correct energy density estimates assigned to the wrong vertical wavenumber.

## ACKNOWLEDGMENTS

## REFERENCES

Briscoe, M. G., 1975: Preliminary results from the tri-moored internal wave experiment (IWEX). *J. Geophys. Res.*, **80**, 3872–3884.

Cairns, J. L., and G. O. Williams, 1976: Internal wave observations from a midwater float, Pt. 2. *J. Geophys. Res.*, **81**, 1943–1950.

D'Asaro, E. A., 1984: Wind forced internal waves in the North Pacific and Sargasso Sea, *J. Phys. Oceanogr*, **14**, 781–794.

Eriksen, C. C., 1985: Implications of ocean bottom reflection for internal wave spectra and mixing. *J. Phys. Oceanogr.*, **15**, 1145–1156.

Fu, L-L., 1981: Observations and models of inertial waves in the deep ocean. *Rev. Geophys. Space Phys.*, **6**, 447–472.

Gargett, A. E., P. J. Hendricks, T. B. Sanford, T. R. Osborn and A. J. Williams III, 1981: A composite spectrum of vertical shear in the upper ocean. *J. Phys. Oceanogr.*, **11**, 1258–1271.

Garrett, C. J. R., and W. H. Munk, 1972: Space-time scales of internal waves. *Geophys. Fluid Dyn.*, **2**, 225–264.

Garrett, C. J. R., and W. H. Munk, 1975: Space-time scales of internal waves: A progress report. *J. Geophys. Res.,* **80,** 291–307.

Gordon, L., 1978: Internal wave climate near the coast of northwest Africa during JOINT-I. *Deep-Sea Res.,* **25,** 625–643.

Gregg, M. C., 1977: Variations in the intensity of small-scale mixing in the main thermocline. *J. Phys. Oceanogr.,* **7,** 436–454.

Hayes, S. P., 1975: Preliminary measurements of the time lagged coherence of vertical temperature profiles. *J. Geophys. Res.,* **80,** 307–311.

Johnson, C. L., and T. B. Sanford, 1980: Anomalous behavior of internal gravity waves near Bermuda. *J. Phys. Oceanogr.,* **10**(12), 2021–2034.

Käse, R., and D. Olbers, 1979: Wind-driven inertial waves observed during Phase III of GATE. *Deep-Sea Res.,* **26,** 191–216.

Katz, E. J., 1975: Tow spectra from MODE. *J. Geophys. Res.,* **80,** 1163–1167.

Kundu, P. K., 1976: An analysis of inertial oscillations observed near Oregon coast. *J. Phys. Oceanogr.,* **6,** 879–893.

Kunze, E., and T. B. Sanford, 1984: Observations of near-inertial waves in a front. *J. Phys. Oceanogr.,* **14,** 566–581.

Kunze, E., and T. B. Sanford, 1986: Near-inertial wave interactions with mean flow and bottom topography near Caryn Seamount. *J. Phys. Oceanogr.,* **16,** 109–120.

Leaman, K. D., 1976: Observations on the vertical polarization and energy flux of near-inertial waves. *J. Phys. Oceanogr.,* **6,** 894–908.

Leaman, K. D., and T. B. Sanford, 1975: Vertical energy propagation of inertial waves: A vector spectral analysis of velocity profiles. *J. Geophys. Res.,* **80,** 1975–1978.

McComas, C. H. III, and F. P. Bretherton, 1977: Resonant interaction of oceanic internal waves. *J. Geophys. Res.,* **82,** 1397–1412.

McComas, C. H. III, and P. Müller, 1981a: Time scales of resonant interactions among oceanic internal waves. *J. Phys. Oceanogr.,* **11,** 139–147.

McComas, C. H. III, and P. Müller, 1981b: The dynamic balance of internal waves. *J. Phys. Oceanogr.,* **11,** 970–986.

MODE Group, 1978: The Mid-Ocean Dynamics Experiment. *Deep-Sea Res.,* **25,** 859–910.

Müller, P., D. Olbers and J. Willibrand, 1978: The IWEX spectrum, *J. Geophys. Res.,* **83,** 479–500.

Munk, W., 1981: Internal waves and small-scale processes. In: *Evolution of Physical Oceanography,* B. Warren and C. Wunsch Eds., MIT Press, Cambridge, MA.

Munk, W., and N. Phillips, 1968: Coherence and band structure of inertial motions in the sea. *Rev. Geophys.,* **6,** 447–472.

Olbers, D., 1983: Models of the oceanic internal wave field, *Rev. Geophys. Space Phys.*, **21**, 1567–1606.

Pedlosky, J., 1979: *Geophysical Fluid Mechanics*. Springer-Verlag, New York, 624 pp.

Perkins, H., 1970: Inertial oscillations in the Mediterranean. Ph.D. thesis, Mass. Inst. of Technol./Woods Hole Oceanogr. Inst., Woods Hole, MA.

Phillips, O. M., 1977: *The Dynamics of the Upper Ocean*, 2nd edition. Cambridge University Press, London, 336 pp.

Pinkel, R., 1975: Upper ocean internal wave observations from FLIP. *J. Geophys. Res.*, **80**, 3892–3910.

Pinkel, R., 1981: On the use of Doppler sonar for internal wave measurements. *Deep-Sea Res.*, **28**, 269–289.

Pinkel, R., 1984: Doppler sonar observations of internal waves: The wave-number frequency spectrum. *J. Phys. Oceanogr.* **14**, 1249–1270.

Pinkel, R., 1985: A wavenumber–frequency spectrum of upper ocean shear. *J. Phys. Oceanogr.*, **15**, 1453–1469.

Pollard, R. T., 1970: On the generation by winds of inertial waves in the ocean. *Deep-Sea Res.*, **17**, 795–812.

Pollard, R. T., 1980: Properties of near-surface inertial oscillations. *J. Phys. Oceanogr.*, **10**, 385–398.

Rossby, H. T., and T. B. Sanford, 1976: A study of velocity profiles through the main thermocline. *J. Phys. Oceanogr.*, **6**, 766–774.

Rubenstein, D., 1988: Scattering of inertial waves by rough bathymetry. *J. Phys. Oceanogr.*, **18**, 5–18.

Sanford, T. B., 1975: Observations of the vertical structure of internal waves. *J. Geophys. Res.*, **80**, 3861–3871.

Sanford, T. B., and N. G. Hogg, 1977: The North Atlantic fine and microstructure cruise *KNORR 52* and *EASTWARD 75-12*. Tech. Rep. 77-11, Woods Hole Oceanogr. Inst., Woods Hole, MA.

Sanford, T. B., R. G. Drever and J. H. Dunlap, 1978: A velocity profiler based on the principles of geomagnetic induction. *Deep-Sea Res.*, **25**, 183–210.

Sanford, T. B., P. G. Black, J. R. Haustein, J. W. Feeney, G. Z. Forristall and J. F. Price, 1987: Ocean response to a hurricane. Part I: Observations. *J. Phys. Oceanogr.*, **11**, 2065–2083.

Stegen, G. R., K. Bryan, J. L. Held and F. Ostapoff, 1975: Dropped horizontal coherence based on temperature profiles in the upper thermocline. *J. Geophys. Res.*, **80**, 3841–3847.

Webster, F., 1968: Observations of inertial-period motions in the deep sea. *Rev. Geophys.*, **6**, 473–490.